A&A, 709, A207 (2026)
https://doi.org/10.1051/0004-6361/202557834

Astronomy & Astrophysics

First study of the supernova remnant population in the Large Magellanic Cloud with eROSITA

II. Spectral analysis and X-ray luminosity function

Federico Zangrandi[1,⋆], Manami Sasaki[1], Knox S. Long[10], Pierre Maggi[6], Miroslav D. Filipović[2], Frank Haberl[3], Patrick Kavanagh[4], Martin Mayer[1], Bärbel Koribalski[5,11], Chandreyee Maitra[3], Sean Points[7], Lister Staveley-Smith[8], Katharina Jurk[1,9], Zachary J. Smeaton[2], and Sara Saeedi[1]

[1] Dr. Karl Remeis Observatory, Erlangen Centre for Astroparticle Physics (ECAP), Friedrich-Alexander-Universität Erlangen-Nürnberg, Sternwartstraße 7, 96049 Bamberg, Germany
[2] School of Science, Western Sydney University, Locked Bag 1797, Penrith, NSW 2751, Australia
[3] Max-Planck-Institut für extraterrestrische Physik, Gießenbachstraße 1, 85748 Garching, Germany
[4] Department of Physics, Maynooth University, Maynooth, Co. Kildare, Ireland
[5] Australia Telescope National Facility, CSIRO, Space and Astronomy, P.O. Box 76, Epping, NSW 1710, Australia
[6] Observatoire Astronomique de Strasbourg, Université de Strasbourg, CNRS, 11 rue de l'Universite , 67000 Strasbourg, France
[7] Cerro Tololo Inter-American Observatory, National Optical Astronomy Observatory, Cassilla 703 La Serena, Chile
[8] International Centre for Radio Astronomy Research (ICRAR), University of Western Australia, 35 Stirling Highway, Perth, WA 6009, Australia
[9] Hamburger Sternwarte, Universität Hamburg, Gojenbergsweg 112, 21029 Hamburg, Germany
[10] Space Telescope Science Institute, 3700 San Martin Drive, Baltimore, MD 21218, USA
[11] Western Sydney University, Locked Bag 1797, Penrith South DC, NSW 2751, Australia

Received 26 October 2025 / Accepted 23 March 2026

ABSTRACT

Aims. Supernova remnants (SNRs) are responsible for the injection of energy and chemical elements into the interstellar medium (ISM). The emission from SNRs can be studied to infer information about the supernova (SN) explosion itself as well as about the properties of the surrounding ISM. Studying a sample of SNRs in a galaxy provides an opportunity to better understand stellar feedback, and the best laboratory for such an investigation is the Large Magellanic Cloud (LMC). The LMC is the nearest star-forming galaxy, it lies outside the Galactic plane line of sight, and therefore its foreground absorption is low.

Methods. The eROSITA telescopes are the best instruments currently available to perform a survey of the SNRs in the entire LMC due to their large field of view and their high sensitivity towards soft X-rays. We used the sample of SNRs reported in the previous paper and performed a spectral analysis on a part of the sample. We estimated the flux and the luminosity of the fainter sources using the energy conversion factor obtained assuming a non-equilibrium ionisation plasma model.

Results. The X-ray luminosity function (XLF) of SNRs in the LMC shows a relatively large number of SNRs at high luminosities. We fitted the distribution with two Gaussian components, which yielded best-fit maxima for the L_X[0.3–8.0 keV] distribution at $m_1 = 10^{34.7\pm0.2}$ erg s^{-1} and $m_2 = 10^{36.5\pm0.4}$ erg s^{-1}. We compared the XLF of the LMC with the XLFs of the Small Magellanic Cloud (SMC), M31, and M33 using a power-law fit and an Anderson-Darling (DA) test. The power indices of the XLFs of the LMC and SMC appear consistent with each other, while those of M33 and M31 are larger. Thus, the latter have steeper power laws, indicating a lower number of X-ray luminous SNRs with respect to the Magellanic Clouds. The DA test showed that the luminosity distributions of SNRs in the SMC and LMC are compatible with being extracted from the same underlying distribution. They are also compatible for different galaxies if we consider the same lower limit for L_X[0.3–8.0 keV] for the entire distribution. Finally, we compared the luminosity and the X-ray sizes (diameter) of the SNRs in our sample. We observed a general trend of anti-correlation between size and X-ray luminosity that can be interpreted as a result of fading with time.

Key words. ISM: general – ISM: supernova remnants

1. Introduction

Supernova remnants (SNRs) are created by the interaction between a supernova explosion (SN) and the interstellar medium (ISM). Therefore, they are an imprint of the stellar feedback on a galaxy. The shock propagates into the ISM, increasing its temperature ($>10^6$ K) and allowing it to emit in the X-ray wavelength. During the expansion, the shock decelerates and produces the so-called reverse shock that propagates inward and heats up the stellar ejecta, which becomes visible in X-rays. The emitting plasma in SNRs is ionised, and usually it is out of ionisation equilibrium.

Absorption by gas and clouds in the Galactic disc complicates the study of SNRs in our own Galaxy, the Milky Way (MW). Therefore, it is difficult to obtain a complete sample of SNRs in the MW. The Large Magellanic Cloud (LMC) is a perfect target for the study of the entire population of SNRs in a galaxy. The Galactic absorption along the line of sight to the LMC is low ($\sim10^{20}$ cm^{-2}, Dickey & Lockman 1990). The LMC, at a distance of 50 kpc (Pietrzyński et al. 2019), is the nearest star-forming galaxy viewed nearly face-on

---

[⋆] Corresponding author: `federico.zangrandi@fau.de` (van der Marel & Cioni 2001) where we expect to find a large population of SNRs.

To understand the connection between the host galaxy and the SNRs in a galaxy, it is important to compare different populations of SNRs in different galaxies. Several X-ray studies have been made on the SNR population in the nearby galaxies. Maggi et al. (2019) performed a spectral analysis on the SNRs in the Small Magellanic Cloud (SMC), where the number of known SNRs is 21. Long et al. (2010) used the ChASeM33 survey, which provides deep *Chandra* data of M33. Despite the depth of the observations and the high angular resolution of *Chandra*, it was not possible to perform a detailed and angular resolved spectral analysis. The flux and luminosity properties were derived from the observed count rate, assuming a non-equilibrium ionisation model (Long et al. 2010). These authors provided the X-ray flux and upper limit of 131 SNRs. Recently, Garofali et al. (2017) combined *XMM-Newton* and *Chandra* data to re-analyse the SNR population of M33, providing another X-ray SNR luminosity function. The M31 SNR population was analysed in the X-ray by Sasaki et al. (2012) using the *XMM-Newton* large programme survey of M31. The authors computed the X-ray flux by converting the count rates of 26 SNRs. More recently, other studies on the SNRs of M31 were performed by Jennings et al. (2014) and Lee & Lee (2014). Both works analysed the SNR population, particularly in the optical band, but they did not provide new measurements on the X-ray flux of new sources. In the LMC, the spectral analysis of 51 SNRs was made by Maggi et al. (2016) using *XMM-Newton*, and it gives a deep view on the spectral properties of the known remnants. Maggi et al. (2016) report that the SNR population in the LMC has the largest number of bright sources ($L_X > 10^{36}$ erg s^{-1}) compared to nearby galaxies. Maggi et al. (2016) argue this is most likely due to the lower metallicity of the stars in the LMC, which causes less mass loss by stellar winds. Another possibility is that the difference in the number of bright objects arises from pure statistical noise. Maggi et al. (2016) already compared the X-ray luminosity functions (XLFs) of SNRs in nearby galaxies, finding no particular difference between the different distributions. Recently, Zangrandi et al. (2024) used the extended Roentgen Survey with an Imaging Telescope Array (eROSITA) all-sky survey (eRASS) data to study the SNR population of the LMC, updating the total number of confirmed SNRs to 77. The advantage of the eROSITA All-sky survey is the capability to provide data from the entire LMC with relatively uniform exposure. This allows an X-ray flux measurement on a larger SNR sample to be performed.

In this study, we explore the flux and luminosity of SNRs in the LMC down to $F_{\rm lim}[0.3–8.0\,{\rm keV}] \sim 3.2 \times 10^{-14}$ erg s^{-1} cm^{-2}, which corresponds to a lower luminosity of $L_{\rm lim}[0.3–8.0\,{\rm keV}] \sim 9.6 \times 10^{33}$ erg s^{-1}. In comparison, the previous study by Maggi et al. (2016) reached a farther lower limit of $L_{\rm lim}[0.3–8.0\,{\rm keV}] \sim 7 \times 10^{33}$ erg s^{-1}. However, comparing the luminosities at the faint end of the distribution is difficult because all luminosities are derived from the spectral analysis by Maggi et al. (2016), while in our case the luminosity of faint sources could only be derived from the count rates. Here, we present a larger sample of sources based on eROSITA, including new SNRs confirmed by Kavanagh et al. (2022) and in paper I. We explore the relationship between the X-ray size and luminosity. With the largest sample of SNRs available to this day, we provide a much more complete overall picture of the SNR XLF in the LMC and extend the results presented in Maggi et al. (2016). We applied the same technique as in Chomiuk & Wilcots (2009) to compare the XLF of SNRs in the nearby galaxies. Chomiuk & Wilcots (2009) systematically compared the radio luminosity function of the SNRs in the Local Group using a maximum likelihood estimator to fit and compare the power index. For the radio luminosity function, Chomiuk & Wilcots (2009) found compatibility between different SNR luminosity functions for different galaxies. In addition, we used a Kolmogorov-Smirnov test to compare the different distributions. In our work, we used both data from Long et al. (2010) and Garofali et al. (2017), considering them both as representative of the SNR distribution in M33. This is the second of a series of papers on the SNRs in the LMC with eROSITA. In the first paper (Zangrandi et al. 2024) we used X-ray data as well as optical and radio data to find new SNRs in the LMC. A third paper on an X-ray morphological study of the SNRs in the LMC is in preparation.

This paper is organised as follows: in Sect. 2, we describe the eROSITA data. The X-ray analysis is described in Sect. 3. In Sect. 4, we report the cross-section matching between SNRs and pulsars in the LMC, and we discuss the implications for the spectral analysis. The discussion on the flux and the luminosity measurements is reported in Sect. 5. The relation between the X-ray size and the X-ray luminosity is reported in Sect. 6. Finally, our conclusions are discussed in Sect. 7. From now on we refer to the first paper as Paper 1.

2. X-ray data

As in Paper 1, the present study was conducted using data from eROSITA in the all-sky survey mode. eROSITA is part of the Spectrum-Roentgen-Gamma (SRG) observatory (Sunyaev et al. 2021). The four all-sky surveys (eRASS:4) provided X-ray data that cover of the entire LMC and its surroundings. eROSITA is composed of seven telescope modules (TMs). Each telescope is composed of 54 nested mirrors with a Wolter-1 configuration, which converge the X-ray photons in a charge-coupled device (CCD) camera. To process the data, we use the eROSITA Science Analysis Software System (eSASS) software (Brunner et al. 2022), version 211214. We create a mosaic event file of the LMC using `evtool`; the mosaic is used to produce the images and extract the spectra. As for Zangrandi et al. (2024) we used the calibrated data version 020.

3. X-ray analysis

3.1. Spectral analysis

We extracted the spectra and created redistribution matrix file (RMF) and ancillary response file (ARF) using the `srctool` task of the eSASS software (Brunner et al. 2022). The spectra extraction was performed separately for the source regions and for the background regions.

The SNR regions were defined by visually inspecting the images and created to contain most of the emission. The background regions were chosen as regions near the sources with a size large enough to ensure a good statistics. We extracted the spectra for TM 1, 2, 3, 4, 6.

We excluded the point sources from the regions. For the point source identification, we used the point source catalogue obtained by the eSASS team using eRASS:4. The pipeline to obtain such a catalogue is described in Merloni et al. (2024). The source catalogue in Merloni et al. (2024) contains point sources dominated by active galactic nuclei (AGNs) and sources detected as extended, dominated by clusters of galaxies. We excluded point sources with at least a detection likelihood `DETLIKE` > 10 if the extension likelihood `EXTLIKE` = 0, and `DETLIKE` > 20 if the `EXTLIKE` > 0.

We used `Xspec` to perform a combined fit using the data from each TM for the source and the background regions. We performed a combined fit to properly distinguish the different contributions from the background and to better constrain the source parameters.

3.2. Background spectrum

The contribution of the background was scaled using a scaling factor defined as the ratio between the geometric extraction areas used for the source region and for the background region, $f_{\mathrm{scale}} = \mathrm{A}_{\mathrm{source}}/\mathrm{A}_{\mathrm{background}}$. The vignetting effects are taken into account by extracting the ARFs for all background and source regions separately.

In general, we used a standard fitting procedure. We started fitting only the background. Once the best fit is found, we froze the background parameters and fitted the source model.

To model the background, we used different contributions (Snowden et al. 2008). At first, the Local hot bubble (LHB) was modelled with a non-absorbed thermal plasma with a typical temperature of $kT = 0.1$ keV, we used one unabsorbed `apec` (Smith et al. 2001). Another background component is the Galactic halo which is usually modelled by two absorbed thermal components the first one 'hot' with a typical temperature between 0.3–0.8 keV which we can call Galactic corona (GC) and one 'cold' component with a typical temperature between 0.1–0.3 keV which we can call circumgalactic medium (CGM). For this reason, we used two absorbed `apec` components where the temperatures and the normalisations were allowed to vary during the fitting process. For the Galactic absorption, we used the line of sight column density measured by Dickey & Lockman (1990). We used the Python package `gdpyc` Gas and Dust Python Calculator[1] to obtain the Galactic column density for the different lines of sight. To take into account the cosmic X-ray background (CXB), we used an absorbed power law with a fixed photon index of $\Gamma = 1.46$ (Lumb et al. 2002; De Luca & Molendi 2004; Moretti et al. 2009). The CXB is caused by the unresolved AGNs in the background.

Another component of the background consists of the solar wind charge exchange (SWCX), which can make an important contribution to low energies. To model this component, we used Gaussian lines. The line width was frozen to 0.0 keV. The modelled SWCX are C VI (0.46 keV), O VII (0.57 keV), O VIII (0.65 keV), O VIII (0.81 keV), Ne IX (0.92 keV), Ne IX (1.02 keV), and Mg VI (1.35 keV) (Snowden et al. 2004). The final model of the background is

$$\mathrm{LHB} + \mathrm{SWCX} + N_{\mathrm{H,\,Gal}}(\mathrm{CGM} + \mathrm{GC} + \mathrm{CXB}). \tag{1}$$

To take into account the contribution from the particle background and instrumental lines, we used the filter wheel closed (FWC) model developed by Yeung et al. (2023) using the FWC data. Since the particle background is not affected by the effective area of the telescope, we folded the FWC model just with the RMF and not with the ARF. In the FWC model, we used a multiplicative constant which was the only free parameter for the particle background, all the other components were frozen to the values derived by Yeung et al. (2023) from FWC data, which were extracted from a detector area of $\mathrm{A}_{\mathrm{FWC}} = 0.82\ \mathrm{deg}^2$. In particular, the particle background becomes dominant at high energy 5.0–10 keV.

3.3. Source spectrum

On top of the background model, we modelled the SNR contribution with at least one thermal component in non-equilibrium ionisation (NEI) model. We used `vnei` (Hamilton et al. 1983; Borkowski et al. 2001) in `Xspec`, where the abundance of several elements can be varied separately.

The plasma in SNRs is often in NEI. Few electron collisions occurred after the shock because of the low densities involved, the electron collisions affect the ionisation of the plasma. The rarity of the ion collisions is the reason that the ion temperature is often not the same as that of the electrons. The main parameters for an NEI model are: temperature (kT), ionisation time scale ($\tau = n_e t$), and the emission measure ($EM \propto n_e^2 V$). We let all three parameters free to vary during the fit.

Each NEI is absorbed by the Galactic column density and by the LMC column density. The latter is due to the absorbing material inside the LMC, and it is another free parameter of the fit. The Galactic absorption was frozen to the value of the column density measured in Dickey & Lockman (1990) as described in Sect. 3.2.

For each source, we took into account the bulk motion of the LMC, fixing the redshift to 9.27×10^{-4} (Richter et al. 1987). Depending on the evolutionary stage of the SNR different abundances can dominate the spectrum. If the ejecta are bright the metal abundances can be more than solar, while if the swept-up ISM dominates, the element abundances will reflect the ISM abundances. For the bright sources, reported in Tables A, we applied the models used in Maggi et al. (2016), while for the fainter sources we assume the spectra are dominated by the swept-up ISM, see Sect. 3.4. The ISM abundances of the LMC are lower than in the MW; for this reason, at first we froze the abundances to 0.5 $\mathrm{Z}_{\odot}$ (Westerlund 1997; Schenck et al. 2016; Hocdé et al. 2023; De Cia et al. 2024, and references within) The solar abundances have been set to `wilm` (Wilms et al. 2000) using `abund` in `Xspec`. Since most of the sources have relatively few counts, we separated the SNRs sample into three categories described in the following Section 3.4. In total, we perform a spectral fit on 39 sources. The spectral results are listed in tables in Appendices A and B.

3.4. Categorising our sample

Bright sources.. This group is composed of the brightest remnants in the sample. We consider sources with at least an average of 1000 net counts per TM. For the 12 sources in this sample, we could perform a relatively detailed spectral analysis, with more than one thermal component. Since for these sources the eROSITA exposure time is not large (2–7 ks), we used the same model as applied by Maggi et al. (2016) using the same number of components with the same abundances which were frozen during the fit, unless residuals were visible. In such cases we allowed the abundance of single element to vary. This was the case for Ne in J0526–6605 and J0535–6602, and for Si and S in J0509–6731. We performed an un-grouped spectral analysis using `c-stat` statistic (Cash 1979) in `Xspec`. From these sources, we could measure the flux and luminosities directly from the spectrum as described in Sect. 5.1. The fitted values are reported in Appendix A.

Medium bright sources.. This group of sources is composed of sources where we had at least 400 net counts combining TM1, 2, 3, 4, and 6. In this case, we could perform a spectral analysis, but not with the same complex models as for the

---

[1] https://gdpyc.readthedocs.io/en/latest/

bright sources. For this reason, we decided to just fit an absorbed thermal NEI ($N_{\rm H} \cdot$ NEI) on top of the background. The abundances were frozen to 0.5 $Z_\odot$ which correspond to the average ISM abundance in the LMC (Westerlund 1997; Schenck et al. 2016; Hocdé et al. 2023; De Cia et al. 2024, and references within). Therefore, we could measure the LMC absorption, the temperature of the plasma, the ionisation time scale, and the normalisation. We did not bin the data, and we used `c-stat` statistic. From these sources, we could measure the flux and luminosity directly from the spectrum as described in Sect. 5.1. We evaluated the errors on each parameter, and we excluded the sources with an error for the normalisation of the thermal component larger than 100%. A total of 27 sources was fitted with a single thermal component. The fit results are reported in Appendix B.

Faint sources.. This group is composed of sources, for which we decided not to perform a spectral analysis. Therefore, we could not derive parameters such as the temperature of the plasma, ionisation time scale, and LMC absorption. Despite this, we estimated the flux, and therefore the luminosity, using an energy conversion factor (ECF) as described in Sect. 5.2.

With the approach described, we were able to estimate the flux and luminosity of all the sources in the sample. However, for the following results we consider only the confirmed SNRs. We consider as significant detection only sources with integrated counts in the energy range 0.3–8.0 keV larger than 3σ above the local background. With these constraints we reach a lower flux of $F_{lo}[0.3\text{–}8.0\,\text{keV}] \sim 3.2 \times 10^{-14}$ erg s^{-1} cm^{-2}, which corresponds to a lower luminosity of $L_{lo}[0.3\text{–}8.0\,\text{keV}] \sim 9.6 \times 10^{33}$ erg s^{-1}.

4. Matching with pulsars

The X-ray emission from SNRs is typically thermal emission. However, for some SNRs, non-thermal emission components have also been detected in their spectrum. This is in particular the case for very young SNRs, in which there are relativistic electrons, which have TeV energies that emit X-ray synchrotron radiation. The synchrotron time-scale is inversely proportional to the electron energy, and therefore these electrons lose their energy in much less time than the less energetic (GeV) electrons, which emit radio synchrotron radiation for a much longer time. In addition, if a neutron star was formed in a CC SN and it is either accreting from a companion or particles are accelerated in its magnetosphere, non-thermal X-rays can be observed as well. Many of these neutron stars show pulsed emission due to their rotation and are called pulsars.

We investigated the spatial distribution of SNRs and that of SNR candidates with the spatial distribution of known pulsars in the LMC. The detection of a pulsar associated with an SNR can provide constrains on the origin of the SNR. Furthermore, if the pulsar is not resolved, it can contribute as a non-thermal component to the spectrum of the SNR. We used the online catalogue of known pulsars provided by the Australia Telescope National Facility (ATNF)[2], catalogue version 2.5.1. We looked for sources located inside a radius of 7 deg around the centre of the LMC. For the centre of the LMC we used the coordinates $\alpha = 80.8$ deg Dec $= -69.8$ deg reported in the NASA/IPAC Extragalactic Database[3], which was measured by de Vaucouleurs et al. (1976). The large radius of 7 deg for the area, which was studied, is based on the recent discoveries of SNR candidates on the outskirts of the LMC (Filipović et al. 2022; Zangrandi et al. 2024; Sasaki et al. 2025). In this region, we found 30 pulsars with positions to be compared with the positions of SNRs and SNR candidates. This search does not take into account that some of these sources might be just on the line of sight of the LMC, and they might not belong to the Magellanic system. According to Manchester et al. (2006), four of them are Galactic sources. The discrimination between Galactic and extragalactic sources can be achieved by measuring the dispersion measure (DM). Sources with DM >25 cm^{-3} pc are considered extragalactic (Cordes & Lazio 2003). Most of the pulsars in the Magellanic Clouds have a DM between 65–150 cm^{-3} pc (Manchester et al. 2006). We excluded the Galactic pulsars from the rest of the analysis. The remaining 26 pulsars are considered the most updated list of pulsars in the LMC (for a discussion on the pulsars in the LMC see: Mazets et al. 1979; Manchester et al. 2006; Kulkarni et al. 2003; Ridley et al. 2013; Johnston et al. 2022; Wang et al. 2022; Hisano et al. 2022). The soft Gamma-Ray Repeater J0526–66 is an X-ray pulsar and has been classified as a magnetar (Mazets et al. 1979; Kulkarni et al. 2003). All the radio pulsar in this list were detected using the Parkes telescope (McCulloch et al. 1983; McConnell et al. 1991; Manchester et al. 1993; Kaspi et al. 1994; Manchester et al. 2006; Ridley et al. 2013). We also included 4XMM J045626.3–694723 which is a second magnetar candidate in the LMC recently found by Imbrogno et al. (2023).

For the pulsars, we use the positional errors reported in the ATNF Pulsar Catalogue for the positional uncertainty for the cross-correlation of the positions. For the SNRs and the SNR candidates in our sample, we use the extent as described in Paper 1 as positional uncertainty. In the case that an SNR has the shape of an ellipse, we used the mean between the semi-major and semi-minor axes as the effective radius. First, we are interested in seeing how many radio pulsars fall inside an SNR. Therefore, we cross-matched the positions of the radio pulsars and the SNRs and selected those pulsars that are located inside the extent of a remnant. However, it has been observed that some neutron stars are fast-moving objects (Gott et al. 1970). One of the reasons for their proper motion is often believed to be the kick received during the supernova explosion, which results in an initial velocity of $\sim$ 400 km s^{-1} (Hobbs et al. 2005). This means that a fast-moving neutron star is located inside an SNR for only a few 10^4 years (Kargaltsev et al. 2017). To evaluate which pulsar is associated with an SNR, we thus have to take into consideration the proper motion of the neutron star. Unfortunately, the proper motion of the pulsars in the LMC has not been measured. Therefore, we used the median value for the transverse velocity reported in Hobbs et al. (2005), where a sample of 233 Galactic pulsars has been analysed. In particular, we are interested in the 2D velocity, which means the magnitude of the velocity projected onto the sky in km s^{-1}, often called the transverse velocity and calculated as $V = \mu_{tot} D$, where μ_{tot} is the observed proper motion ($\sim$ milli-arcsec yr^{-1}) and D is the distance to the source. Hobbs et al. (2005) calculated a median velocity of 139 km s^{-1} for the entire sample of Galactic pulsars and a median velocity of 142 km s^{-1} for the pulsars which can be associated with Galactic SNRs. These velocities have been corrected for stellar motions and for the Galactic rotation (Hobbs et al. 2005). Since their sample size for pulsars in SNRs is relatively small, with only seven pulsars, we decided to use the median velocity of 139 km s^{-1} instead of 142 km s^{-1}. Combining the age and the speed of the pulsar, we evaluated the travelled distance d by the neutron star. To calculate the travelled distance, we use the pulsar age as reported in the ATNF catalogue. The age has been calculated using the characteristic age of the

---

[2] https://www.atnf.csiro.au/research/pulsar/psrcat/

[3] https://ned.ipac.caltech.edu/

pulsar, $\tau_c = P/2\dot{P}$, where P is the measured rotational period and $\dot{P}$ is its time derivative. It assumes that the neutron star rotation slows down due to magnetic dipole radiation, and therefore the initial rotational period must have been larger than the current period (Hobbs et al. 2005). However, this is a simplification as this estimate will result in an incorrect age for a non-dipole magnetic field. Furthermore, neutron stars can be rejuvenated by accretion from a companion star, forming a milli-second pulsar (Bhattacharya & van den Heuvel 1991). We note that none of the pulsars in this sample has a rotational period of milliseconds. We converted the expected travelled distance into angular distance, assuming the LMC at 50 kpc distance from us. An SNR located inside a circle with a radius d around a pulsar has likely been produced in the same supernova as the neutron star. We searched for an overlap of the circle within the travel distance of a pulsar with the extent of an SNR. If the overlap area is more than 0.0%, we consider it a match. One should note that the older pulsars in the catalogue have ages of millions of years, while the time for which an SNR is visible is about an order of magnitude smaller (Blondin et al. 1998). For this reason, we calculated the travelled distance only for pulsars with an age of less than 10^5 years. However, not all the pulsars have an estimated age. In such a case we could not estimate how far the pulsar had travelled since its birth. We thus found seven pulsars, which match the position of SNRs: J0451–6717, J0456–6950, J0526–6605, J0529–6653, J0537–6910, J0538–6921, and J0540–6920. We note that J0451–6717, J0456–6950 and J0538–6921 result in a match due to the large uncertainty on the positions of the radio pulsar, about 7 arcmin (Ridley et al. 2013). It means that 26% of the sample of known pulsars in the LMC are located in an SNR in the LMC, which implies that only 5.6% of the SNRs and candidates contain a radio pulsar. Among the new SNRs and SNR candidates proposed in Paper 1 only J0451–6717 is associated with a pulsar. On the one hand this supports the idea that most of the new SNRs and SNR candidates can be type Ia. On the other hand, there are several reasons why no pulsars are detected in other candidates. One reason could be that the beamed radiation of the pulsar is not pointing towards the observer, or the radiation of the central compact object is too dim to be detected. Using the pulsar age to define the search radius gives a conservative upper limit in the fraction of pulsars matching. Therefore, we assumed an age of 100 kyr for all pulsars. In this case, the matching number decreases to 5, which corresponds to 18.5% of the known pulsars in the LMC. The SNRs with geometrical matching are: J0451–6717, J0526–6605, J0529–6653, J0537–6910, and J0540–6920.

In Fig. 1, we show all the pulsar/SNR matches with red crosses. Even considering the travelled distance, only seven pulsars can be associated with SNRs. The yellow markers instead show what type of SNR is associated with these pulsars. Three out of five are confirmed CC SNR, and most likely, these pulsars have been produced by these explosions. The other two sources, which are associated with type Ia SNRs, can be chance coincidences. The underlying image in Fig. 1 shows the distribution of the H I surface brightness (Kim et al. 1998).

We used the matches to investigate whether we found a non-thermal emission component in the spectral analysis. We used an additional absorbed power-law component to the NEI component. For the SNR candidate J0451–6717, spectral analysis was not possible, as the source only has a net count of 375, which is less than our threshold. In 2024 (Obs: 0921550101, PI: F. Haberl) this source was observed with *XMM-Newton* and the analysis is on-going (Haberl et al., in prep.). Also, for the SNR J0456–6950, the net count of 17 is not enough to perform a spectral fit. Even though SNR J0537–6910 is known to contain a pulsar wind nebula, the spectral fit does not improve with an additional power-law component. Therefore, we conclude that the photon statistics of our data are not good enough to resolve all the components. Also in the spectrum of J0538–6921, the additional power-law component does not improve the fit.

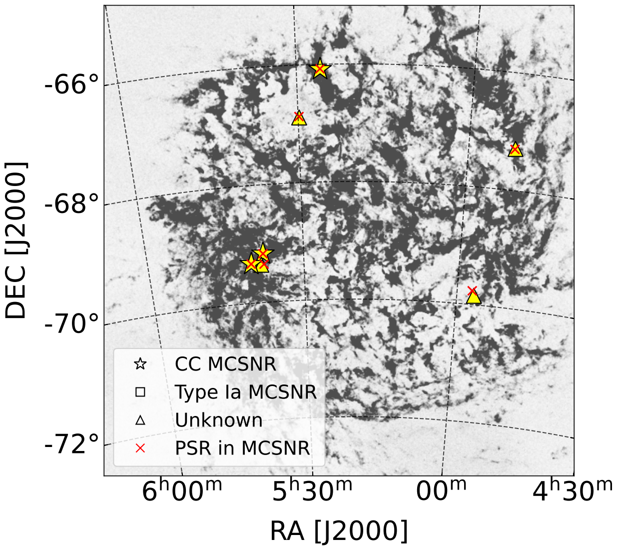

Fig. 1. Spatial distribution of the SNRs with matched pulsars overlayed onto the H I surface brightness map of Kim et al. (1998). The yellow markers show the positions of the SNRs with a match, distinguishing between core-collapse (stars), type Ia (squares), and unknown SNR explosion types (triangles). The red crosses show the position of the matched pulsars.

The SNR J0526–6605, also known as N49, is known to contain a point source, known as PSR B0525-66. In our spectrum, we included a power-law component as in Maggi et al. (2016) and Park et al. (2012). We froze the photon index to 2.5 as in Park et al. (2012). For J0529–6653 and J0540–6920, the fit improves with the addition of a power law. In these cases, the photon index Γ was left free to vary. The fitted values are $\Gamma = 2.43^{+0.37}_{-0.27}$ and $\Gamma = 1.99^{+0.05}_{-0.03}$, respectively.

5. Flux and luminosity

In this section, we describe how we derived the luminosity of the entire sample. To summarise, for bright and medium bright sources (see Sect. 3.4) the flux and luminosity are directly measured from the spectrum (see Sect. 3.1). For the faint sources, we estimated the flux and the luminosity from the count rate using an ECF (see Sect. 5.2). In both cases, the luminosity is obtained from the flux by assuming the same distance for all the SNRs, $D_{\mathrm{LMC}} \sim 50$ kpc (Pietrzyński et al. 2019), and using the relation $L = 4\pi D^2_{\mathrm{LMC}}\,F$. Unless otherwise stated, all fluxes and luminosities reported are absorbed.

5.1. Bright and medium bright sources

For 39 sources of the sample, we obtained the flux from the spectral analysis. The model used in the spectral analysis is described in Sect. 3.1. The fitted values are reported in Appendices A and B. The flux is calculated for the NEI component in the spectral model using the `flux` command in `Xspec` in the energy interval

0.3–8.0 keV. During the flux calculation, the background components were set to zero. The errors on the flux were calculated using the Markov chain Monte Carlo implemented in `Xspec`. Since we simultaneously fit TM12346, we take the average flux from the five TMs and propagate the errors of the individual fluxes on the mean value. As shown in Paper 1 the eROSITA luminosities are compatible with previous *XMM-Newton* results (Maggi et al. 2016).

5.2. Faint sources

The estimated flux for the fainter sources is obtained by multiplying the mean measured count rate per TM in the energy band 0.3–8.0 keV by an ECF. The error of the flux is derived from the error on the count rate.

To calculate the ECF we used `Xspec`, assuming a single temperature `vnei` with $kT = 0.60\,\mathrm{keV}$, $N_{\mathrm{H}}^{\mathrm{LMC}} = 0.0\,\mathrm{cm}^{-2}$, and $\tau = 3 \times 10^{10}\,\mathrm{s\,cm}^{-3}$. We simulated a spectrum using the eROSITA on-axis RMF and ARF. We calculated the model flux and the corresponding predicted count rate in the energy band of 0.3–8.0 keV. We then divided the model flux (F) by the predicted count rate (R) to get the ECF: ECF $= F/R = 5.77 \times 10^{-12}\,\mathrm{erg\,cm}^{-2}\,\mathrm{count}^{-1}$.

The choice of the spectral parameters is based on the values obtained from the spectral fit of the 21 medium bright sources ($L < 10^{35}\,\mathrm{erg\,s}^{-1}$). For these sources, the fits result in a median plasma temperature of $kT = 0.60\,\mathrm{keV}$ and a median ionisation time scale of $\tau = 3\times10^{10}\,\mathrm{s\,cm}^{-3}$. It is noted that the temperatures measured with our model are larger than those reported in Maggi et al. (2016). For sources with $L < 10^{35}\,\mathrm{erg\,s}^{-1}$ we measure a median plasma temperature of $kT = 0.60\,\mathrm{keV}$, while Maggi et al. (2016) derived a median temperature of $kT = 0.31\,\mathrm{keV}$. It is worth noting that the difference arise from the different models used. Maggi et al. (2016) used a collisional ionisation equilibrium (CIE) model (`apec`), while in this work we used an NEI for all sources. The NEI model naturally skewed the temperature high, since lower ionisation time scale means lower ionisation for a given temperature. Comparing the ECFs calculated with the mean temperature in Maggi et al. (2016) and the same ionisation time scale as stated above, we measure a difference of <1% between the two ECFs, while the average error on the fluxes is ∼11%. This shows that the statistical errors are larger than the systematic errors.

5.3. Flux and luminosity distributions

Figure 2 shows the distribution of luminosities of the SNR sample. Since we assumed all SNRs in the LMC are at the same distance, the fluxes and luminosities follow the same distribution. We measure a median flux of $\log(F_{\mathrm{median}}) = -12.7$ and a median luminosity of $\log(L_{\mathrm{median}}) = 34.9$. We calculate the modes of the distributions at $\log(F_{\mathrm{mode}}) = -12.8$, and $\log(L_{\mathrm{mode}}) = 34.8$. Fig. 2 shows a main peak towards the faint tail of the distribution. In addition, a second peak between $10^{36}\,\mathrm{erg\,s}^{-1}$ and $10^{37}\,\mathrm{erg\,s}^{-1}$ seems to be present. For this reason, we fit the distribution with a combination of two Gaussians. The fit was performed by minimising a negative log-likelihood as

$$\sum \left(y_{\mathrm{model}} - y_{\mathrm{obs}} \cdot \log(y_{\mathrm{model}})\right), \tag{2}$$

where y_{model} is

$$y_{\mathrm{model}} = A_1 \exp\left[-\frac{(x-\mu_1)^2}{2\sigma_1^2}\right] + A_2 \exp\left[-\frac{(x-\mu_2)^2}{2\sigma_2^2}\right]. \tag{3}$$

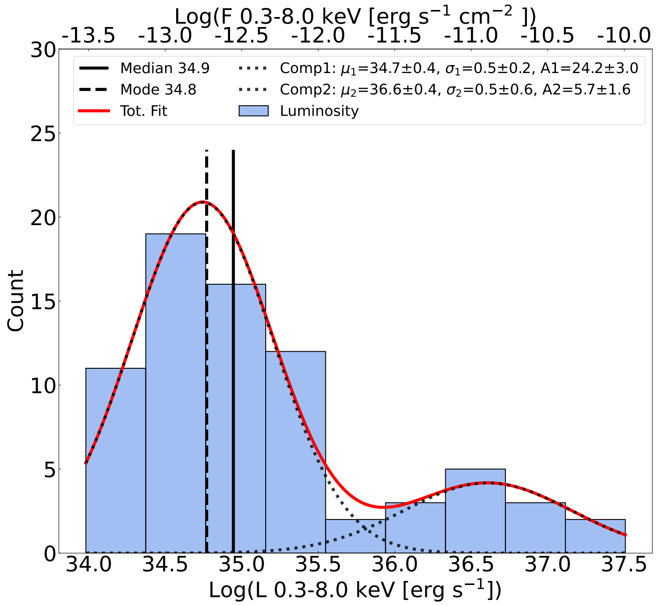

Fig. 2. Histogram of the luminosity and flux in the energy band of 0.3–8.0 keV for the SNRs and SNR candidates in the LMC. The solid red line shows the best fit of the distribution with the dashed lines indicating the two Gaussian components of the best fit.

The normalisations of the Gaussian components depend on the data binning, while the best fit $\mu_1 = 34.7 \pm 0.2$ and $\mu_2 = 36.5 \pm 0.4$ are independent from the data binning. The maxima in the luminosity distribution are at $m_1 = 10^{34.7\pm0.2}\,\mathrm{erg\,s}^{-1}$ and $m_2 = 10^{36.6\pm0.4}\,\mathrm{erg\,s}^{-1}$.

5.4. Luminosity function

An efficient way to compare the different SNR populations is to compare the cumulative XLF, which is a measure on how many SNRs are observed above a certain luminosity. To be consistent with Maggi et al. (2016) we used the absorbed flux. Furthermore, they have shown that the cumulative XLF is not significantly affected by absorption since the foreground absorption is relatively small. We compare the XLF of the LMC with the XLFs of the SNRs in the Local Group, such as the SMC (Maggi et al. 2019), M31 (Sasaki et al. 2012), and M33 (Long et al. 2010; Garofali et al. 2017). For M33, we used the catalogue provided in Long et al. (2010) and the updated catalogue reported in Garofali et al. (2017). In the following, we refer to them as L10 and G17. For G17, we used the fluxes reported in their table and we converted them to luminosities assuming a distance of 817 kpc (Freedman et al. 2001), which is the same distance assumed both in L10 and G17. Since the luminosities in M31 and M33 were measured in the energy range of 0.3–2.3 keV we converted them to 0.3–8.0 keV. For M31 Sasaki et al. (2012) assumed a CIE model with a temperature of $kT = 0.2\,\mathrm{keV}$, and the fluxes were calculated unabsorbed. The same CIE model but with $kT = 0.6\,\mathrm{keV}$ was assumed to calculate the luminosities in L10. In G17, the reported flux is the sum of the measured fluxes obtained using the `emldetect` for `pn`, `MOS1`, and `MOS2`. We divided the flux by 3 to obtain a mean flux. They assumed the same model as L10 to obtain the ECF used in `emldetect` task. The fluxes of the SMC were obtained by spectral fitting (Maggi et al. 2019). To compare the XLFs in different galaxies, we need to convert all luminosities to a common model. We re-fitted the LMC sources using an absorbed `apec` and we determined the

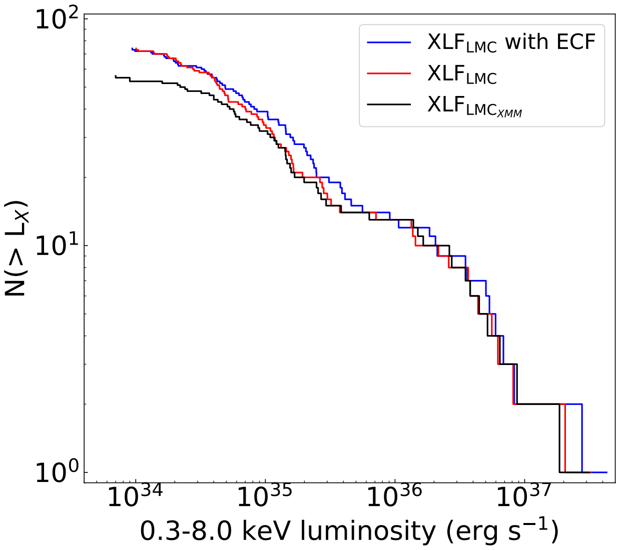

Fig. 3. Comparison between the cumulative XLF of the LMC. The XLF obtained in Maggi et al. (2016) is shown in black, while the eROSITA XLF for which the luminosities were determined as described in Sect. 5.1 is shown in red, and the eROSITA luminosities obtained using the ECF assuming an `apec` model with $kT = 0.5$ keV and $N_{\rm H} = 0.25 \times 10^{22}$ cm^{-2} are in blue.

median fitted temperature and median fitted absorption: $kT = 0.5$ keV and $N_{\rm H}^{\rm LMC} = 0.25 \times 10^{22}$ cm^{-2}. Using these values, we calculated the difference in flux between the models assumed in Sasaki et al. (2012), L10, G17, and in Maggi et al. (2019). We followed the same procedure described in Sect. 5.2 to calculate a new ECF $\sim 5.46 \times 10^{-12}$ erg cm^{-2} count^{-1}, for the model `apec` $kT = 0.5$ keV and $N_{\rm H}^{\rm LMC} = 0.25 \times 10^{22}$ cm^{-2}. In this way, we obtained comparable fluxes for all galaxies in the energy band 0.3–8.0 keV. In Fig. 3 we compare the XLF of the LMC for Maggi et al. (2016), in which the luminosities were obtained by fitting *XMM-Newton* spectra (black curve), and for the eROSITA luminosities. The red XLF is obtained by fitting the spectra of the sources with net counts > 400, and using an ECF for the remaining sources (see Sect. 5.2). Finally, the XLF assuming an `apec` model and converting the count rate into luminosity using an ECF for all the sources is shown in blue. The red and black curves in Fig. 3 are comparable over a large range of luminosities, except for the faintest tail where our catalogue has more sources. The blue curve in Fig. 3 seems to be shifted to higher luminosities above $\sim 5 \times 10^{34}$ erg s^{-1}. This suggests that the simple assumed `apec` model tends to overestimate the luminosity with respect to the freely fitted spectra. The increased sample size of 71 SNR in the LMC XLF in respect to Maggi et al. (2016) allows us to provide a more complete view on the LMC SNR XLF. It is worth mention that since it is difficult to correct the XLF for sensitivity (see below), the comparison between eROSITA and *XMM-Newton* at the faintest end should be taken cautiously.

Figure 4a shows the XLFs for different galaxies. There are differences in the lower limit of each sample: LMC $\sim 9.6 \times 10^{33}$ erg s^{-1}, SMC $\sim 4.9 \times 10^{33}$ erg s^{-1}, M33 $\sim 1.0 \times 10^{34}$ erg s^{-1} and M31 $\sim 1.7 \times 10^{35}$ erg s^{-1}. The lower luminosity limit for the Magellanic Clouds is expected due to the smaller distance of the SMC (~60 kpc Hilditch et al. 2005) and LMC (~50 kpc Pietrzyński et al. 2019) compared to M33 and M31. However, despite M31 being closer than M33, the minimum observed luminosity in M31 is larger. The distance of M31 is ~744 kpc (Vilardell et al. 2010), while that of M33 is 805–817 kpc (Freedman et al. 2001; Scowcroft et al. 2009). We attribute this discrepancy to an observational bias of SNR detections, most likely due to the different inclinations of the two galaxies, and possible difference in exposure times and different instruments. The inclination of M31 is $i \sim 71°$ while that of M33 is $i \sim 54°$ (De Vaucouleurs et al. 2013). A greater inclination angle leads to a higher probability for confusion and also to a higher column density along the line of sight, which, in turn, leads to higher absorption of the fainter sources. We expect old SNRs to become fainter and more X-ray soft, for which the absorption is more significant. From Fig. 4a, the XLF of the LMC appears to have a peculiar shape. As in Maggi et al. (2016), we find an excess of remnants at higher luminosities. The excess at higher luminosity in the LMC XLF is probably related to the high luminosity peak visible in Fig. 2 (see Sect. 5.1 for the discussion).

Regarding the completeness of the eROSITA detections, a comprehensive study on the completeness of the eRASS1 survey has been presented by Seppi et al. (2022). This study evaluates the efficiency of the eROSITA source detection algorithm, explained in Merloni et al. (2024), as a function of exposure time and source flux for both AGNs (which are point sources) and clusters of galaxies (extended). For exposure times larger than 400 seconds, the completeness of 80% is calculated for galaxy clusters at a flux limit of 4.75×10^{-13} erg s^{-1} cm^{-2}, while that for AGNs has a flux limit at 1.92×10^{-14} erg s^{-1} cm^{-2}. Unfortunately, a quantitative evaluation of the relation between completeness and flux for SNRs is not straightforward. Most of the remnants in our catalogue were detected from visual inspections of LMC surveys in different wavelengths (see Zangrandi et al. 2024). Furthermore, the evaluation of the completeness would require a comparison with a simulated mock catalogue of SNRs, which is not trivial to compile. However, from the shape of the LMC XLF, we argue that our sample is not complete at the low-luminosity end of the distribution.

Since each galaxy has different properties, such as different stellar masses and different star formation rates (SFRs), we normalise the XLF by the SFR of the host galaxy. There are several tracers to estimate the SFR of a galaxy. For a comparison of their consistency in the local volume, see Lee et al. (2009) and Catalán-Torrecilla et al. (2015). We decided to use the SFR reported in Karachentsev et al. (2013) derived from the Hα flux. To derive the SFR they used the linear relation from Kennicutt (1998):

$$\text{SFR}[M_\odot\,\text{yr}^{-1}] = 0.945 \times 10^9\; F(\text{H}\,\alpha)\; D^2, \tag{4}$$

where $F(\text{H}\,\alpha)$ is the line flux in [erg s^{-1} cm^{-2}] and D is the distance of the galaxy in Mpc. The SFRs for the galaxies discussed in our comparison are listed in Table 1. Figure 4b shows that when the XLF of M33 and M31 is normalised to the galaxy's SFR, they tend to occupy the same region of the plot. Instead, the normalised XLFs of the LMC and SMC show a larger fraction of luminous SNRs for $L \gtrsim 10^{35}$ erg s^{-1} compared to M33 and M31.

In general, cumulative distributions are often modelled assuming an underlying power law distribution (Chomiuk & Wilcots 2009; Long et al. 2010; Sasaki et al. 2012). A common way to evaluate if a cumulative distribution function can be described by a power law distribution is to plot it in a log-log diagram and see if it follows a linear relation. In that case, the slope should be the index of the power law.

As pointed out in Clauset et al. (2009), a linear regression of a log-log cumulative function is not a good estimator for the

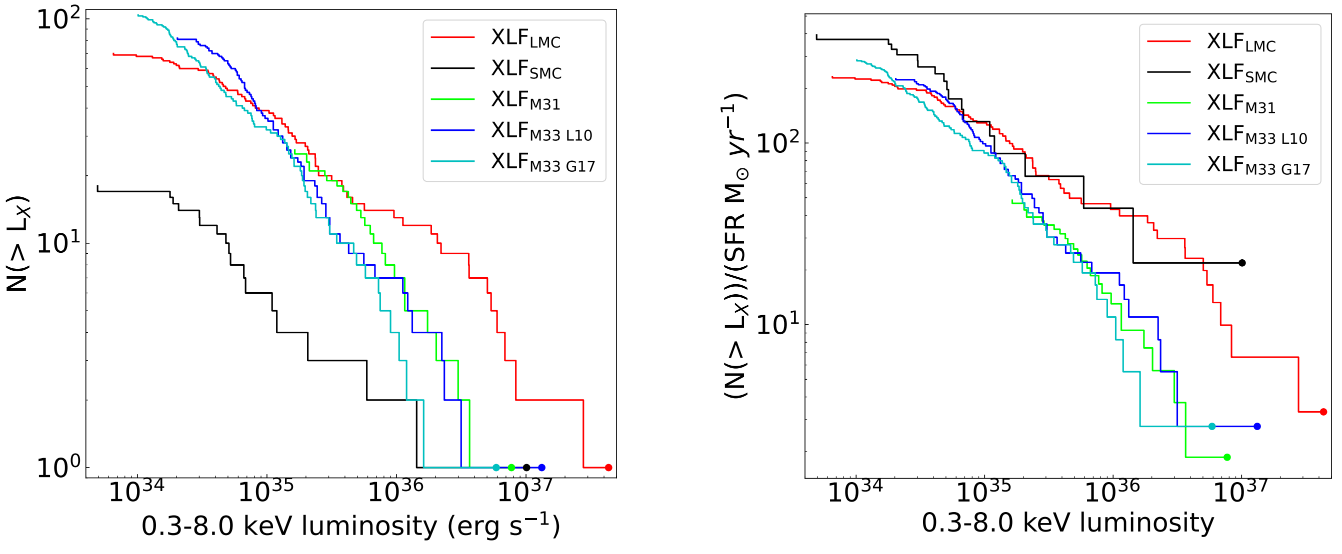

(a) **(b)**

Fig. 4. (a) Comparison between the cumulative XLF in the Local Group. (b) Comparison between the cumulative XLF in the Local Group normalised by the SFR of the hosting galaxy.

Table 1. Best-fit power-law slope α and $L_{\rm min}$. The SFR is from Karachentsev et al. (2013).

Galaxy	SFR ($M_\odot$/yr)	α	$L_{\rm min}$ (erg s^{-1})
LMC	0.30	1.51 ± 0.07	5.94×10^{34}
SMC	0.05	1.65 ± 0.17	2.80×10^{34}
M31	0.54	2.04 ± 0.25	3.92×10^{35}
M33 L10	0.36	1.85 ± 0.11	5.04×10^{34}
M33 G17	0.36	1.63 ± 0.06	1.33×10^{34}

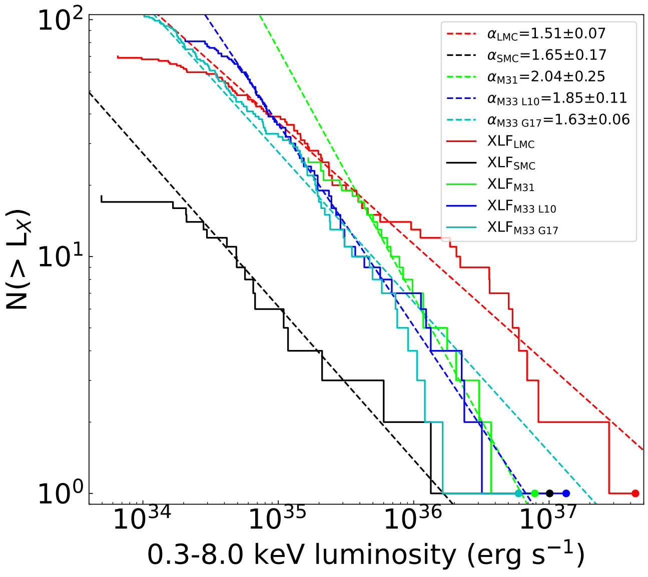

Fig. 5. Comparison between the cumulative XLF in the Local Group. The dotted lines show the best-fit power law.

power-law index. In this case, the fit will be dominated by the tail of the distribution with a higher probability, here, the low luminosity tail. Clauset et al. (2009) discuss a more robust estimator for the power-law index and its error based on the maximum likelihood estimator expressed in Eq. (5),

$$\alpha = 1 + n\left[\sum_{i=1}^{n} \ln \frac{L_i}{L_{\rm min}}\right]^{-1}, \; \sigma = \frac{\alpha - 1}{\sqrt{n}}, \tag{5}$$

where $L_{\rm min}$ is the minimum value for which the power-law behaviour is valid and the sum of Eq. (5) is performed for the luminosities larger than $L_{\rm min}$. The existence of a lower bound, $L_{\rm min}$, is due to observational limits. The value of $L_{\rm min}$ can be estimated using a Kolmogorov-Smirnov statistic. The basic idea is to find $L_{\rm min}$, which minimises the distance between the distribution of the data and the best fit. This technique is implemented in the Python package `powerlaw` described in Alstott et al. (2014). We utilised this package to evaluate and compare α and $L_{\rm min}$ of the XLF distributions of the different galaxies. The fit was performed following the maximum likelihood estimator on the entire sample of each galaxy. The results are reported in Table 1. Fig. 5 shows the XLFs with the relative best-fit power-law.

We notice that the power-law indices of the SMC, M33 L10, and M31 are compatible within one sigma error. Further, the power-law indices of the LMC, SMC, and M33 G17 agree within one sigma error. Nevertheless, the power-law index of the LMC is the lowest and this is probably due to the fact that the LMC XLF distribution is not well described by a simple power-law distribution. Using the Python package `powerlaw`, we tested if each of these distributions could be better described by other model distributions such as lognormal, exponential, or truncated power laws. None of these showed a significant improvement in the fit. To evaluate whether each observed XLF is likely drawn from the same underlying distribution, we perform a null-hypothesis test, under the null hypothesis that the two compared distributions are sampled from the same underlying distribution. For such tests, the Kolmogorov-Smirnov test is often used. The Kolmogorov–Smirnov test encounters challenges in detecting differences in the compared distributions when these occur near the end or the beginning of the distributions

Table 2. Results of luminosity distribution comparisons using the DA test.

Galaxy pairs	DA p-value	Comp	DA p-value$_{\rm cut}$	Comp
LMC vs SMC	0.14	Y	>0.25	Y
LMC vs M31	<0.01	N	0.22	Y
LMC vs M33 L10	0.04	N	0.14	Y
LMC vs M33 G17	<0.01	N	0.05	Y
SMC vs M31	<0.01	N	>0.25	Y
SMC vs M33 L10	0.02	N	>0.25	Y
SMC vs M33 G17	>0.25	Y	0.19	Y
M31 vs M33 L10	<0.01	N	0.14	Y
M31 vs M33 G17	<0.01	N	0.10	Y

Notes. The first column shows the galaxy pair considered for the test. The second column shows the results, in p-values, considering the entire catalogue of SNRs in both galaxies. The third column summarises if the two distribution are likely draw from the same underling (Y) or not (N). The last two columns show the test results, including only luminosities larger than 1.7×10^{35} erg s^{-1}.

(Feigelson & Babu 2012, see). To avoid this problem, we used the Anderson-Darling test (DA) (Anderson & Darling 1952; Scholz & Stephens 1987), implemented in python through the `SciPy`[4] package. We used $p < 0.05$ to reject the null-hypothesis, that means the two distributions are not sampled from the same underlying distribution. The p-values are reported in Table 2. First we ran the DA test on the entire sample in each galaxy, and therefore the distributions have different lower limits. Our DA test results show that the SNR luminosity distributions of the LMC, SMC are compatible to each other, that means we cannot reject the null-hypothesis. Instead, comparing the other distributions the DA test allows us to reject the null-hypothesis. These differences can arise from the incompleteness of the samples. Therefore, we repeated the DA test only considering luminosities above the minimum luminosity of M31 1.7×10^{35} erg s^{-1}, in this case, all the distributions do not show statistically significant differences between each other, with the only exception of SMC versus M33 G17. The results of the test are reported in Table 2. It is worth to compare these results with Fig. 4b, where we normalised the XLFs by the SFR. The excess of SNRs in the LMC and SMC with respect to the other galaxies can be an indication of an intrinsically larger population of luminous SNRs.

5.5. Group of luminous SNRs

It is interesting to look closely to the bright 'bump' of the luminosity function. The number of SNRs with $L \geq 10^{36}$ erg s^{-1} is 13. The existence of such a luminous population was already known (Maggi et al. 2016), and due to their brightness they have been typed. 31% of the group is composed by confirmed type Ia SNRs (J0505–6753, J0509–6731, J0509–6844, J0519–6902), while the remaining 69% are confirmed CC (J0453–6829, J0505–6802, J0525–6559, J0525–6938, J0526–6605, J0535–6602, J0535–6916, J0537–6910, J0540–6920). The classification as type Ia or CC is complicated and mainly based on the ejecta abundances. This is usually possible for young and bright remnants. In addition, in CC there might be a contribution to the luminosity due to the presence of a neutron star. It is interesting to note that all the bright type Ia SNRs in this sample are Balmer-dominated remnants (Tuohy et al. 1982), which have very strong Hα lines but weak [O III] and [S II] lines. Since most of the extragalactic SNRs outside the Milky Way system are detected using the [S II]/Hα ratio, it is possible that the brightest type Ia SNRs in more distant galaxies are missed. Furthermore, the SNRs in M33 and M31 are usually not spatially resolved, and the brightest remnants could be difficult to detect due to confusion with other diffuse emission. For these two reasons the lack of bright remnant of galaxies such as M31 and M33 may be due to observational biases. However Lin et al. (2020) did not find any Balmer dominated SNR in M33 with $L_{\rm X} > 10^{35}$ erg s^{-1}, despite taking into account observational biases such as ionisation conditions, gas fraction and metallicity.

6. Luminosity-size relation

Assuming that all the sources are located at the same distance, which is the LMC distance, allows us to convert the angular size (diameter) to the physical size of the remnant. It is interesting to compare the size of the remnant and its luminosity. In general, the X-ray luminosity is proportional to the square of the pre-shock density and to plasma emissivity, the so-called cooling function Λ. The cooling function depends on plasma temperature and plasma abundances. In SNRs, the luminosity depends on the evolutionary state of the remnant and varies over time.

A similar study was made by Ou et al. (2018), where they compared the radio size and the X-ray luminosity of 59 SNRs. We instead compared the X-ray size with the X-ray luminosity of the source using the most recent catalogue of Paper 1. Assuming that the remnants are in Sedov–Taylor phase (Sedov 1959), which corresponds to adiabatic expansion, it is possible to write the relation between the size and the age of the remnant as

$$R_S = 1.15 \left(\frac{E_0 \, t^2}{\rho_0} \right)^{1/5}, \qquad (6)$$

where E_0 is the explosion energy and ρ_0 is the pre-explosion mass density. The mass density can be written as $\rho_0 = \bar{m}_n n_0$, with n_0 the particle number density and $\bar{m}_n$ the mean nucleon mass. To calculate the luminosity, we used $E_0 = 10^{51}$ erg. The ambient density of the ISM can vary of orders of magnitude from cold and dense gas ($n_0 \sim 10$ cm^{-3}) to warm or hot rarefied gas ($n_0 \sim 0.01$ cm^{-3}) (Draine 2011). Since the CC SNRs originate from massive stars, we expect the pre-explosion density to have a quite complex structure due to stellar winds and photoionisation from the massive progenitor.

In Fig. 6, we show the comparison between the physical size and the luminosity of the SNRs and the candidates. Since the angular resolution of eROSITA is relatively low, with an average FoV resolution of 26 arcsec (Predehl et al. 2021), when possible we used the sizes derived from *XMM-Newton* and reported in Maggi et al. (2016), Kavanagh et al. (2016), and Kavanagh et al. (2022). For the rest of the sample, we used the size derived from the eROSITA images. In Fig. 6 we separate the SNRs according to their origin, CC or type Ia, as reported in Maggi et al. (2016). The dashed black lines in Fig. 6 show the luminosity predicted by assuming a Sedov–Taylor phase with constant density. In general, the X-ray luminosity can be calculated as

$$L = \Lambda n_e n_{\rm H} V, \qquad (7)$$

---

[4] `https://docs.scipy.org/doc/scipy/reference/generated/scipy.stats.anderson_ksamp.html`

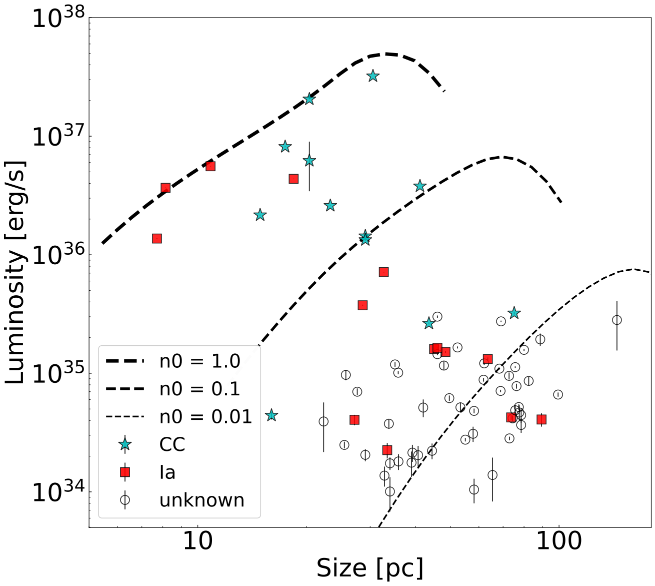

Fig. 6. Luminosity and size comparison. The luminosity is measured in the energy band 0.3–8.0 keVas described in Sect.5.1. The size is from *XMM-Newton* observations (Maggi et al. 2016; Kavanagh et al. 2016, 2022). The dashed lines follow the theoretical luminosity-size relation assuming the Sedov–Taylor phase and different initial ambient densities.

where Λ is the cooling function, V is the volume of emission, and n_e and $n_{\rm H}$ are the number densities of electrons and protons of the emitting gas, respectively. The number densities of electrons and of protons are related to each other in the following way: $\xi = n_e/n_{\rm H} = 1.20$, assuming that all the H and He atoms are ionised. To estimate the theoretical curves we used a similar approach used in Long (2017). Thus, we used `XSPEC`, in particular the `sedov` model (Borkowski et al. 2001). In the Sedov–Taylor phase, the shock temperature depends on the velocity of the shock, and when calculating the time derivative of Eq. (6), we obtained Eq. (8)

$$v_S = \frac{2}{5}\frac{R_S}{t}, \tag{8}$$

from which we calculated the temperature of the shock as a function of time (= radius) according to Eq. (9),

$$T_S = \frac{3}{16}\mu m_p v_S^2/k_B, \tag{9}$$

where $\mu = 1.4$ is the mean molecular weight, while k_B is the Boltzmann constant. The temperature decreases due to the adiabatic expansion. We assumed strong shock approximation and in this case, the post-shock density is $n_{\rm ps} = 4n_0$ where, n_0 is the pre-shock number density. The ionisation time $\tau = n_e t$, where n_e is the electron density which is estimated using $n_e = \xi n_{\rm ps}$. The emission measure (EM) is defined as EM $= \int n_e n_{\rm H} dV \sim \xi n_{\rm ps} V f$, where $f < 1$ is the filling factor, and V is the volume given by the Sedov–Taylor shock radius. Thus the volume is a function of time. Assuming redshift $z = 0$, the EM is connected to the normalisation of the `XSPEC` models as norm $= 10^{-14}\,\frac{\rm EM}{4\pi\,D^2}$, where D is the distance in cm. We simulated the spectrum as function of time (= radius) using the temperature, ionisation time, and normalisation as described above fixing the abundances to $0.5\,Z_\odot$. Since in our model we are simulating the emission is dominated by the shock we used a filling factor $f = 0.25$ to account that not the entire volume is emitting and that mass is conserved. In this case we assumed a distance of $D_{\rm LMC} = 50\,$kpc, and we estimated the flux and therefore the luminosity in the energy range (0.3–8.0 keV) for different initial densities. As the evolution depends on the initial conditions and the X-ray luminosity as well as on the size (= time), the luminosity is calculated for each size and pre-shock density. In Fig. 6, the curves show that higher n_0 predict higher luminosity, as expected from the squared dependency in Eq. (7). We noticed that the `sedov` implemented in `Xspec` is calculated for temperatures $80\,{\rm keV} > kT > 0.09\,{\rm keV}$. Therefore, the curves do not cover the entire plot.

The emitting volume V is related to the size of the remnant, and in the Sedov–Taylor phase, the luminosity increases with the size because the volume of the emitting plasma increases with time. During the adiabatic expansion the temperature decreases. For temperatures below about 10^7 keV most of the emission is line emission in UV (Cox & Daltabuit 1971), shifting the spectrum to lower energies, which makes it more susceptible to absorption. Therefore we expect a drop in the observed X-ray flux. When the radiative losses become important the adiabatic expansion ends. The shocked gas decreases its temperature and therefore the luminosity decreases. According to Blondin et al. (1998), the timescale to enter the radiative phase can be estimated as

$$t_{rad} \sim 2.9 \times 10^4\ E_{51}^{4/17}\ n_0^{-9/17}\ {\rm yr}, \tag{10}$$

where E_{51} is the explosion energy in units of 10^{51} erg and n_0 is the pre-shock density in units of cm^{-3}. The remnant after the radiative phase will slowly merge with the ISM. This implies that the relation between the size of the remnant and its X-ray luminosity, predicted in the adiabatic phase, will come to an end. The SNRs are broadly distributed in Fig. 6, but there is a decreasing trend between the luminosity and the size. In our modelling we do not consider the contribution of the ejecta, which may underestimate the emission of smaller size SNRs.

We can propose two possible interpretations of Figure 6. The first is that most SNRs are expanding into very low density gas since the bulk of the SNRs lie below the 0.01 cm^{-3} curve. The other possibility is that most of these SNRs are already in the radiative phase, and so their X-ray luminosities are well below the Sedov phase prediction. The best way to distinguish which of the two possibility is more likely would be to measure the expansion velocities of the shock.

7. Conclusions

In this work, we have investigated the X-ray luminosity distribution of the SNR population in the LMC. With the largest available sample of SNRs in the LMC, the results of our study draw a more complete picture of the XLF of the SNRs in the LMC. We performed a spectral analysis on the brightest SNRs, with at least 400 net counts. We measured the X-ray luminosity for these sources. For the faintest sources, the X-ray luminosity was obtained by multiplying the net count rate by an ECF. The ECF was obtained assuming a single NEI model, with $kT = 0.60\,$keV, $N_{\rm H}^{\rm LMC} = 0.0\,{\rm cm}^{-2}$, and $\tau = 3\times10^{10}\,{\rm s\,cm}^{-3}$. Our main conclusions are the following:

1. The X-ray luminosity distribution of SNRs in the LMC can be described by two Gaussian components with the two peaks at $m_1 = 10^{34.7\pm0.2}\,{\rm erg\,s}^{-1}$ and $m_2 = 10^{36.5\pm0.4}\,{\rm erg\,s}^{-1}$;
2. We computed the cumulative XLF and compared it with the XLF of SNRs in the nearby galaxies SMC, M31, and M33. We normalised the XLFs with the SFR of the host galaxy

and found that the XLFs of M31 and M33 are consistent with each other, while the XLFs of the Magellanic clouds tend to be higher at higher luminosities. This suggests a possible larger population of luminous SNRs in the Magellanic Clouds;

3. We fitted the XLFs with a power law using a maximum likelihood estimator, and we compared the best-fit indexes. For the LMC we fitted an index $\alpha = 1.51 \pm 0.07$. We find that the LMC index is incompatible within a 1σ error with the indices of M31 and M33 using the catalogue in Long et al. (2010) (M33 L10). The index of the SMC and M33, using the Garofali et al. (2017) (M33 G17) catalogue, have a compatible index with the LMC, within the errors;
4. Using a DA test on the entire sample for each galaxy, we find that the X-ray luminosity distributions of the LMC and SMC do not show a statistically significant difference between each other, while for other galaxies the DA test gives a p-value of <0.05, suggesting that it is unlikely that the observed SNR luminosity distribution is sampled by the same underlying probability distribution as in the other galaxies. We repeated the test using only luminosities larger than 3.92×10^{35} erg s^{-1} and find that the DA test shows that there is no statistical difference between the SNR luminosity distribution in different galaxies. Our interpretation is that for distant galaxies with a large inclination, such as M31, the XLF is distorted by the selection effects, which prevent us from observing the less luminous and fainter SNRs. On the other hand, in the more distant galaxies (M31 and M33), we may not detect the bright SNRs either due to confusion in the nuclear region of the galaxies, which prevent us from resolving them from the bright diffuse emission. The DA test is affected by the different ranges in luminosities of the different distributions;
5. Assuming a Sedov–Taylor solution, we compared the theoretical X-ray luminosity-size relation with the observed X-ray luminosity-size relation, separating between CC and type Ia SNRs. We generally observed a trend for an inverse correlation between the physical size of the SNR and its X-ray luminosity.

Data availability

The spectra corresponding to Appendix C are available at the CDS via `https://cdsarc.cds.unistra.fr/viz-bin/cat/J/A+A/709/A207`.

Acknowledgements. This work was supported by the Deutsche Forschungsgemeinschaft through the projects SA 2131/14-1 and SA 2131/14-2. M.S. acknowledges support from the Deutsche Forschungsgemeinschaft through the grants SA 2131/13-1, SA 2131/15-1, and SA 2131/15-2. P.J.K. acknowledges support from the Research Ireland Pathway programme under Grant Number 21/PATH-S/9360. The paper is based on data from eROSITA, the soft X-ray instrument aboard *SRG*, a joint Russian-German science mission supported by the Russian Space Agency (Roskosmos), in the interests of the Russian Academy of Sciences represented by its Space Research Institute (IKI), and the Deutsches Zentrum für Luft- und Raumfahrt (DLR). The *SRG* spacecraft was built by Lavochkin Association (NPOL) and its subcontractors and is operated by NPOL with support from the Max-Planck Institute for Extraterrestrial Physics (MPE). The development and construction of the eROSITA X-ray instrument were led by MPE, with contributions from the Dr. Karl Remeis Observatory Bamberg, the Erlangen centre for Astroparticle Physics (ECAP), the University of Hamburg Observatory, the Leibniz Institute for Astrophysics Potsdam (AIP), and the Institute for Astronomy and Astrophysics of the University of Tübingen, with the support of DLR and the Max Planck Society. The Argelander Institute for Astronomy of the University of Bonn and the Ludwig Maximilians Universität Munich also participated in the science preparation for eROSITA. The eROSITA data shown here were processed using the eSASS/NRTA software system developed by the German eROSITA consortium. Part of this work was supported by the German Deutsche Forschungsgemeinschaft, DFG project number Ts 17/2–1. This research has made use of Aladin, SIMBAD and VizieR, operated at the CDS, Strasbourg, France. This paper includes archived data obtained through the Parkes Pulsar Data archive on the CSIRO Data Access Portal (`http://data.csiro.au`.)

References

Alstott, J., Bullmore, E., & Plenz, D. 2014, PLoS One, 9, 1
Anderson, T. W., & Darling, D. A. 1952, Ann. Math. Statist., 193
Bhattacharya, D., & van den Heuvel, E. 1991, Phys. Rep., 203, 1
Blondin, J. M., Wright, E. B., Borkowski, K. J., & Reynolds, S. P. 1998, ApJ, 500, 342
Borkowski, K. J., Lyerly, W. J., & Reynolds, S. P. 2001, ApJ, 548, 820
Brunner, H., Liu, T., Lamer, G., et al. 2022, A&A, 661, A1
Cash, W. 1979, ApJ, 228, 939
Catalán-Torrecilla, C., De Paz, A. G., Castillo-Morales, A., et al. 2015, A&A, 584, A87
Chomiuk, L., & Wilcots, E. M. 2009, ApJ, 703, 370
Chomiuk, L., & Wilcots, E. M. 2009, The Astrophysical Journal, 703, 370
Clauset, A., Shalizi, C. R., & Newman, M. E. J. 2009, SIAM Rev., 51, 661
Cordes, J. M., & Lazio, T. J. W. 2003, NE2001.I. A New Model for the Galactic Distribution of Free Electrons and its Fluctuations
Cox, D. P., & Daltabuit, E. 1971, ApJ, 167, 113
De Cia, A., Roman-Duval, J., Konstantopoulou, C., et al. 2024, A&A, 683, A216
De Luca, A., & Molendi, S. 2004, A&A, 419, 837
de Vaucouleurs, G., de Vaucouleurs, A., & Corwin, J. R. 1976, Second reference catalogue of bright galaxies, 1976, 0
De Vaucouleurs, G., De Vaucouleurs, A., Harold Jr, G., et al. 2013, Third Reference Catalogue of Bright Galaxies, 3 (Springer Science & Business Media)
Dickey, J. M., & Lockman, F. J. 1990, ARA&A, 28, 215
Draine, B. T. 2011, Physics of the Interstellar and Intergalactic Medium, 19 (Princeton University Press)
Feigelson, E. D., & Babu, G. J. 2012, Modern Statistical Methods for Astronomy: with R Applications (Cambridge University Press)
Filipović, M. D., Payne, J. L., Alsaberi, R. Z. E., et al. 2022, MNRAS, 512, 265
Freedman, W. L., Madore, B. F., Gibson, B. K., et al. 2001, ApJ, 553, 47
Garofali, K., Williams, B. F., Plucinsky, P. P., et al. 2017, MNRAS, 472, 308
Gott, III, J. R., Gunn, J. E., & Ostriker, J. P. 1970, ApJ, 160, L91
Hamilton, A. J. S., Sarazin, C. L., & Chevalier, R. A. 1983, ApJS, 51, 115
Hilditch, R. W., Howarth, I., & Harries, T. 2005, MNRAS, 357, 304
Hisano, S., Crawford, F., Bonidie, V., et al. 2022, ApJ, 928, 161
Hobbs, G., Lorimer, D. R., Lyne, A. G., & Kramer, M. 2005, MNRAS, 360, 974
Hocdé, V., Smolec, R., Moskalik, P., Ziółkowska, O., & Singh Rathour, R. 2023, A&A, 671, A157
Imbrogno, M., Israel, G. L., Rodríguez Castillo, G. A., et al. 2023, MNRAS, 524, 5566
Jennings, Z. G., Williams, B. F., Murphy, J. W., et al. 2014, ApJ, 795, 170
Johnston, S., Parthasarathy, A., Main, R. A., et al. 2022, MNRAS, 509, 5209
Karachentsev, I. D., Makarov, D. I., & Kaisina, E. I. 2013, AJ, 145, 101
Kargaltsev, O., Pavlov, G. G., Klingler, N., & Rangelov, B. 2017, J. Plasma Phys., 83, 635830501
Kaspi, V. M., Johnston, S., Bell, J. F., et al. 1994, ApJ, 423, L43
Kavanagh, Sasaki, M., Bozzetto, L. M., et al. 2016, A&A, 586, A4
Kavanagh, P. J., Sasaki, M., Filipović, M. D., et al. 2022, MNRAS, 515, 4099
Kennicutt, Jr., R. C. 1998, ARA&A, 36, 189
Kim, S., Staveley-Smith, L., Dopita, M. A., et al. 1998, ApJ, 503, 674
Kulkarni, S. R., Kaplan, D. L., Marshall, H. L., et al. 2003, ApJ, 585, 948
Lee, J. H., & Lee, M. G. 2014, ApJ, 786, 130
Lee, J. C., Gil de Paz, A., Tremonti, C., et al. 2009, ApJ, 706, 599
Lin, C. D.-J., Chu, Y.-H., Ou, P.-S., & Li, C.-J. 2020, ApJ, 900, 149
Long, K. S. 2017, in Handbook of Supernovae, eds. A. W. Alsabti, & P. Murdin, 2005
Long, K. S., Blair, W. P., Winkler, P. F., et al. 2010, ApJS, 187, 495
Lumb, D. H., Warwick, R. S., Page, M., & Luca, A. D. 2002, A&A, 389, 93
Maggi, P., Haberl, F., Kavanagh, P. J., et al. 2016, A&A, 585, A162
Maggi, P., Filipović, M. D., Vukotić, B., et al. 2019, A&A, 631, A127
Manchester, R. N., Fan, G., Lyne, A. G., Kaspi, V. M., & Crawford, F. 2006, ApJ, 649, 235
Manchester, R. N., Mar, D. P., Lyne, A. G., Kaspi, V. M., & Johnston, S. 1993, ApJ, 403, L29
Mazets, E. P., Golentskii, S. V., Ilinskii, V. N., Aptekar, R. L., & Guryan, I. A. 1979, Nature, 282, 587
McConnell, D., McCulloch, P. M., Hamilton, P. A., et al. 1991, MNRAS, 249, 654

McCulloch, P. M., Hamilton, P. A., Ables, J. G., & Hunt, A. J. 1983, Nature, 303, 307
Merloni, A., Lamer, G., Liu, T., et al. 2024, A&A, 682, A34
Moretti, A., Pagani, C., Cusumano, G., et al. 2009, A&A, 493, 501
Ou, P.-S., Chu, Y.-H., Maggi, P., et al. 2018, ApJ, 863, 137
Park, S., Hughes, J. P., Slane, P. O., et al. 2012, ApJ, 748, 117
Pietrzyński, G., Graczyk, D., Gallenne, A., et al. 2019, Nature, 567, 200
Predehl, Andritschke, R., Arefiev, V., et al. 2021, A&A, 647, A1
Richter, O. G., Tammann, G. A., & Huchtmeier, W. K. 1987, A&A, 171, 33
Ridley, J. P., Crawford, F., Lorimer, D. R., et al. 2013, MNRAS, 433, 138
Sasaki, M., Pietsch, W., Haberl, F., et al. 2012, A&A, 544, A144
Sasaki, M., Zangrandi, F., Filipović, M., et al. 2025, A&A, 693, L15
Schenck, A., Park, S., & Post, S. 2016, AJ, 151, 161
Scholz, F. W., & Stephens, M. A. 1987, J. Am. Statist. Assoc., 82, 918
Scowcroft, V., Bersier, D., Mould, J. R., & Wood, P. R. 2009, MNRAS, 396, 1287
Sedov, L. I. 1959, Similarity and Dimensional Methods in Mechanics
Seppi, R., Comparat, J., Bulbul, E., et al. 2022, A&A, 665, A78
Smith, R. K., Brickhouse, N. S., Liedahl, D. A., & Raymond, J. C. 2001, ApJ, 556, L91
Snowden, S. L., Collier, M. R., & Kuntz, K. D. 2004, ApJ, 610, 1182
Snowden, S. L., Mushotzky, R. F., Kuntz, K. D., & Davis, D. S. 2008, A&A, 478, 615
Sunyaev, R., Arefiev, V., Babyshkin, V., et al. 2021, A&A, 656, A132
Tuohy, I. R., Dopita, M. A., Mathewson, D. S., Long, K. S., & Helfand, D. J. 1982, ApJ, 261, 473
van der Marel, R. P., & Cioni, M.-R. L. 2001, AJ, 122, 1807
Vilardell, F., Ribas, I., Jordi, C., Fitzpatrick, E. L., & Guinan, E. F. 2010, A&A, 509, A70
Wang, Y., Murphy, T., Kaplan, D. L., et al. 2022, ApJ, 930, 38
Westerlund, B. E. 1997, The Magellanic Clouds
Wilms, J., Allen, A., & McCray, R. 2000, ApJ, 542, 914
Yeung, M. C. H., Freyberg, M. J., Ponti, G., et al. 2023, A&A, 676, A3
Zangrandi, F., Jurk, K., Sasaki, M., et al. 2024, A&A, 692, A237

Appendix A: Spectral fit results – bright

Table A.1. Spectral fit parameters

MCSNR	N_H [10^{22} cm^{-2}]	kT [keV]	O	Ne	Mg	Si	S	Ar	Ca	Fe	τ [10^{11} s cm^3]	F_X [10^{-13} erg s^{-1} cm^{-2}]
J0505–6753												
Comp1	$0.07^{+0.04}_{-0.02}$	$0.46^{+0.04}_{-0.15}$	0.26	0.40	0.49	0.0	0.0	0.5	0.5	0.0	$0.48^{+1.11}_{-0.07}$	73.0±0.7
Comp2		$0.72^{+0.02}_{-0.01}$	0.0	0.0	0.0	1.03	1.27	0.0	0.0	1.21	282^{+130}_{-177}	64.6±0.6
Comp3		$0.08^{+0.01}_{-0.01}$	0.0	0.0	0.0						$0.01^{+0.01}_{-0.01}$	8.3±0.7
J0505–6802												
Comp1	$0.16^{+0.02}_{-0.01}$	$0.80^{+0.05}_{-0.06}$	0.50	0.50	0.50	0.50	0.50	0.50	0.50	0.50	$0.78^{+0.13}_{-0.07}$	44.1±0.9
Comp2		$0.21^{+0.01}_{-0.02}$	0.11	0.16	0.18	0.37	0.50	0.50	0.50	0.20	$11.0^{+126}_{-1.64}$	42.7±0.8
J0509–6731												
Comp1	$0.14^{+0.02}_{-0.02}$	$0.72^{+0.05}_{-0.04}$	0.0	0.0	0.0	$7.47^{+1.18}_{-0.90}$	$12.3^{+2.5}_{-2.0}$	0.0	0.0	$0.68^{+0.10}_{-0.08}$	$0.15^{+0.02}_{-0.03}$	31.4±0.6
Comp2		$0.23^{+0.01}_{-0.01}$	0.50	0.50	0.50	0.50	0.50	0.50	0.50	0.50	<356	14.4±0.6
J0509–6844												
Comp1	$0.33^{+0.03}_{-0.02}$	$0.87^{+0.02}_{-0.02}$	0.25	1.71	0.33	2.84	3.48	5.26	9.51	1.10	$3.95^{+0.84}_{-0.44}$	118.5±1.2
Comp2		$1.33^{+0.19}_{-0.13}$									364^{+78}_{-262}	29.5±1.5
Comp3		$0.30^{+0.01}_{-0.01}$	0.5	0.5	0.5	0.5	0.5	0.5	0.5	0.5	471^{+14}_{-407}	38.4±0.8
J0519–6902												
Comp1	$0.16^{+0.02}_{-0.01}$	$1.13^{+0.08}_{-0.08}$	0.0	0.0	0.0	0.0	0.0	0.0	0.0	Pure	$0.75^{+0.14}_{-0.11}$	54.5±1.1
Comp2		$0.54^{+0.03}_{-0.04}$	0.50	0.50	0.50	0.50	0.50	0.50	0.50	0.50	489^{+9}_{-67}	25.8±1.0
Comp3		$1.11^{+0.09}_{-0.08}$	0.0	0.0	0.0	0.0	0.0	0.0	0.0	Pure	$1.06^{+0.11}_{-0.19}$	22.5±0.9
Comp4		$0.45^{+0.06}_{-0.10}$	0.0	0.0	0.0	0.0	0.0	0.0	0.0	Pure	298^{+54}_{-37}	11.4±0.7
Comp5		$0.40^{+0.05}_{-0.05}$	Pure	0.0	0.0	0.0	0.0	0.0	0.0	0.0	$0.63^{+0.14}_{-0.16}$	6.1±0.4
Comp6		$0.08^{+0.01}_{-0.01}$	0.0	0.0	0.0	0.0	0.0	1.33	1.33	0.0	148^{+19}_{-27}	2.3±0.3
J0525–6559												
Comp1	$0.27^{+0.01}_{-0.01}$	$0.51^{+0.02}_{-0.03}$	0.07	0.27	0.43	0.34	0.50	0.50	0.50	0.10	$1.49^{+0.23}_{-0.13}$	74.2±0.7
Comp2		$0.21^{+0.01}_{-0.01}$	0.50	0.50	0.50	0.50	0.50	0.50	0.50	0.50	344^{+129}_{-287}	52.5±0.5
J0525–6938												
Comp1	$0.03^{+0.01}_{-0.01}$	$0.85^{+0.01}_{-0.01}$	0.05	0.46	0.19	0.39	0.5	0.5	0.5	0.28	$2.73^{+0.17}_{-0.07}$	763.4±3.0
Comp2		$0.25^{+0.01}_{-0.01}$	9.03	0.25	2.59	1.37	1.03	0.5	0.5	0.15	481^{+7}_{-422}	219.0±1.7
Comp3		$0.43^{+0.01}_{-0.01}$	0.0	0.0	0.0	0.0	0.0	5.29	2.20	1.0	$500^{+2.16}_{-405}$	92.8±2.0
J0526–6605												
Comp1	$0.35^{+0.20}_{-0.01}$	$0.85^{+0.02}_{-0.02}$	0.30	0.42	0.52	1.00	0.50	0.50	0.50	0.41	$2.21^{+0.38}_{-0.58}$	106.0±0.9
Comp2		$0.23^{+0.01}_{-0.01}$		$0.22^{+0.02}_{-0.02}$							$25.8^{+0.12}_{-0.09}$	93.8±0.8
J0535–6602												
Comp1	$0.22^{+0.01}_{-0.03}$	$0.70^{+0.01}_{-0.01}$	$0.70^{+0.10}_{-0.27}$	$1.98^{+0.02}_{-0.11}$	0.85	0.76	0.48	0.14	0.50	$0.40^{+0.01}_{-0.02}$	373^{+91}_{-252}	534.9±1.6
Comp2	$0.08^{+0.01}_{-0.01}$	$0.25^{+0.01}_{-0.01}$	$0.37^{+0.07}_{-0.01}$	0.57	0.12	0.13	0.50	0.50	0.50	0.28	$13.7^{+16.2}_{-1.33}$	161.3±1.1

Table A.1. Continued.

MCSNR	N_H [10^{22} cm^{-2}]	kT [keV]	O	Ne	Mg	Si	S	Ar	Ca	Fe	τ [10^{11} s cm^{3}]	F_X [10^{-13} erg s^{-1} cm^{-2}]
J0535–6916												
Comp1	$0.18^{+0.01}_{-0.01}$	$2.09^{+0.39}_{-0.17}$	0.23	0.76	0.68	0.90	0.65	0.50	0.50	0.31	328^{+145}_{-285}	34.6±1.0
Comp2		1.15									440^{+38}_{-415}	16.7±0.7
Comp3		$0.71^{+0.04}_{-0.06}$									$1.43^{+0.28}_{-0.19}$	20.9±0.6
J0540–6920[a]												
Comp1	$0.67^{+0.04}_{-0.02}$	$0.55^{+0.07}_{-0.26}$	0.50	0.50	0.50	0.50	0.50	0.50	0.50	0.50	316^{+155}_{-280}	3.0±0.5
J0540–6944[b]												
Comp1	$1.26^{+0.09}_{-0.26}$	$0.21^{+0.02}_{-0.05}$	0.50	0.50	0.50	0.50	0.50	0.50	0.50	0.50	$1.27^{+471}_{-0.03}$	1.3±0.1

Notes. The flux from the single component are not absorbed.[a] To account for the pulsar PSR 0540-69 a power-law model was also used with a `PhotonIndex`=$1.99^{+0.05}_{-0.03}$, yielding an unabsorbed flux of F_X = (269.5 ± 1.6) × 10^{-13} erg s^{-1} cm^{-2}.[b] The model include a powerlaw with `PhotonIndex`=$2.43^{+0.10}_{-0.19}$, F_X = (18.3 ± 0.7) × 10^{-13} erg s^{-1} cm^{-2}. In this case the power-law accounts for the straight light contribution from the nearby high mass X-ray binary LMC X-1.

Appendix B: Spectral fit results assuming a single temperature model

Table B.1. Spectral fit results assuming a single temperature model.

MCSNR	N_H [10^{22} cm^{-2}]	kT [keV]	τ [10^{11}s cm^{-3}]	F_X [10^{-14} erg s^{-1} cm^{-2}]	stat	dof
J0450–7050	$0.05^{+0.17}_{-0.04}$	$0.29^{+0.02}_{-0.04}$	$40.6^{+429}_{-14.7}$	27.5 ± 1.4	2324.0	4426
J0453–6655	< 0.04	$0.75^{+0.27}_{-0.19}$	$0.17^{+0.09}_{-0.06}$	40.5 ± 1.1	2062.0	4426
J0453–6829	$0.02^{+0.01}_{-0.01}$	$0.96^{+0.08}_{-0.07}$	$0.12^{+0.01}_{-0.01}$	480.5 ± 3.5	1970.0	4426
J0454–6713	< 0.01	$0.42^{+0.02}_{-0.03}$	306^{+170}_{-266}	55.2 ± 1.1	2154.0	4426
J0456–6533	< 0.04	$0.43^{+0.22}_{-0.10}$	$0.30^{+0.30}_{-0.17}$	13.9 ± 0.8	2998.0	4426
J0506–6541	$0.02^{+0.04}_{-0.02}$	$0.19^{+0.01}_{-0.01}$	396^{+78}_{-361}	22.1 ± 0.9	3895.0	4426
J0506–7026	< 0.03	$0.58^{+0.04}_{-0.05}$	$2.13^{+0.98}_{-0.41}$	44.1 ± 1.3	2553.0	4426
J0508–6902	< 0.03	$0.68^{+0.05}_{-0.07}$	298^{+178}_{-263}	14.2 ± 0.6	1704.0	4426
J0513–6912	< 0.07	$0.70^{+0.07}_{-0.06}$	$1.85^{+471}_{-3.59}$	16.1 ± 0.7	2217.0	4426
J0518–6939	< 0.03	$1.04^{+0.29}_{-0.29}$	$0.14^{+0.07}_{-0.03}$	33.8 ± 1.0	1940.0	4426
J0519–6926	< 0.01	$1.73^{+0.36}_{-0.49}$	$0.08^{+0.02}_{-0.01}$	100.5 ± 2.2	2513.0	4426
J0523–6753	$0.04^{+0.08}_{-0.03}$	$1.23^{+0.27}_{-0.16}$	$0.66^{+0.17}_{-0.16}$	29.5 ± 1.1	2612.0	4426
J0527–6550	< 0.01	$0.54^{+0.18}_{-0.05}$	$0.33^{+0.07}_{-0.14}$	36.6 ± 0.6	3465.0	4426
J0529–6653	$0.015^{+0.04}_{-0.002}$	$0.21^{+0.02}_{-0.01}$	< 282	1.2 ± 0.5	2578.0	4426
J0530–7008	< 0.1	$0.30^{+0.02}_{-0.03}$	378^{+95}_{-346}	26.1 ± 1.2	3009.0	4426
J0531–7100	$0.03^{+0.03}_{-0.02}$	$1.08^{+0.29}_{-0.20}$	$0.17^{+0.06}_{-0.04}$	88.1 ± 1.6	2252.0	4426
J0532–6732	$0.03^{+0.02}_{-0.02}$	$1.17^{+0.28}_{-0.21}$	$0.10^{+0.03}_{-0.02}$	91.7 ± 1.3	3343.0	4426
J0534–6955	$0.20^{+0.02}_{-0.03}$	$0.69^{+0.08}_{-0.03}$	$0.21^{+0.02}_{-0.03}$	238.4 ± 1.7	2436.0	4426
J0534–7033	< 0.01	$0.86^{+0.02}_{-0.03}$	276^{+202}_{-234}	53.6 ± 1.5	2463.0	4426
J0536–7039	< 0.01	$0.67^{+0.04}_{-0.05}$	$1.29^{+0.28}_{-0.20}$	50.7 ± 1.1	2719.0	4426
J0537–6910	$1.57^{+0.03}_{-0.03}$	$2.18^{+0.17}_{-0.13}$	$0.04^{+0.01}_{-0.01}$	446 ± 8.0	3591.0	4426
J0538–6921	< 0.03	$1.01^{+1.28}_{-0.17}$	$0.59^{+0.30}_{-0.36}$	3.03 ± 0.15	3147.6	4426
J0539–7001	$0.11^{+0.07}_{-0.05}$	$0.49^{+0.03}_{-0.05}$	380^{+97}_{-336}	23.7 ± 0.5	2488.0	4426

Table B.1. Spectral fit results assuming a single temperature model.

MCSNR	N_H [10^{22} cm^{-2}]	kT [keV]	τ [10^{11} s cm^{-3}]	F_X [10^{-14} erg s^{-1} cm^{-2}]	stat	dof
J0543–6858	$0.35^{+0.07}_{-0.08}$	$0.96^{+0.46}_{-0.23}$	$0.08^{+0.02}_{-0.01}$	52.7 ± 1.1	3327.0	4426
J0547–6941	$0.38^{+0.07}_{-0.05}$	$0.97^{+0.04}_{-0.04}$	$1.76^{+0.46}_{-0.31}$	54.9 ± 1.0	2055.0	4426
J0547–6943	$0.28^{+0.14}_{-0.07}$	$0.91^{+0.15}_{-0.1}$	$0.9^{+0.20}_{-0.29}$	48.5 ± 1.0	2605.0	4426
J0547–7025	$0.50^{+0.05}_{-0.05}$	$0.68^{+0.07}_{-0.08}$	$0.22^{+0.05}_{-0.03}$	125.2 ± 1.5	2422.0	4426
J0550–6823	< 0.04	$0.77^{+0.10}_{-0.10}$	$0.33^{+0.08}_{-0.07}$	37.7 ± 0.5	4027.0	4426
J0614–7251	< 0.02	$0.60^{+0.23}_{-0.16}$	$0.15^{+0.11}_{-0.05}$	20.6 ± 0.7	1986.0	4426

Notes. The reported absorbed flux is calculated in the energy range 0.3 – 8.0 keV. In MCSNR J0529–6653 we used an additional power law with $\Gamma = 2.43^{+0.37}_{-0.27}$ with an unabsorbed flux $F_X = (2.7 \pm 0.5) \times 10^{-13}$ erg s^{-1} cm^{-2}.

Appendix C: MCSNR spectra

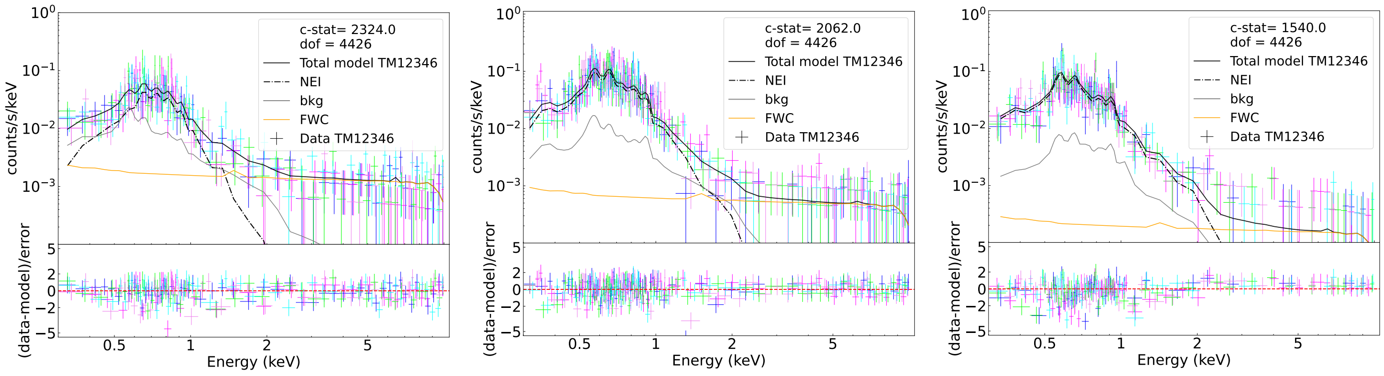

(a) J0450-7050 **(b) J0453-6655** **(c) J0454-6626**

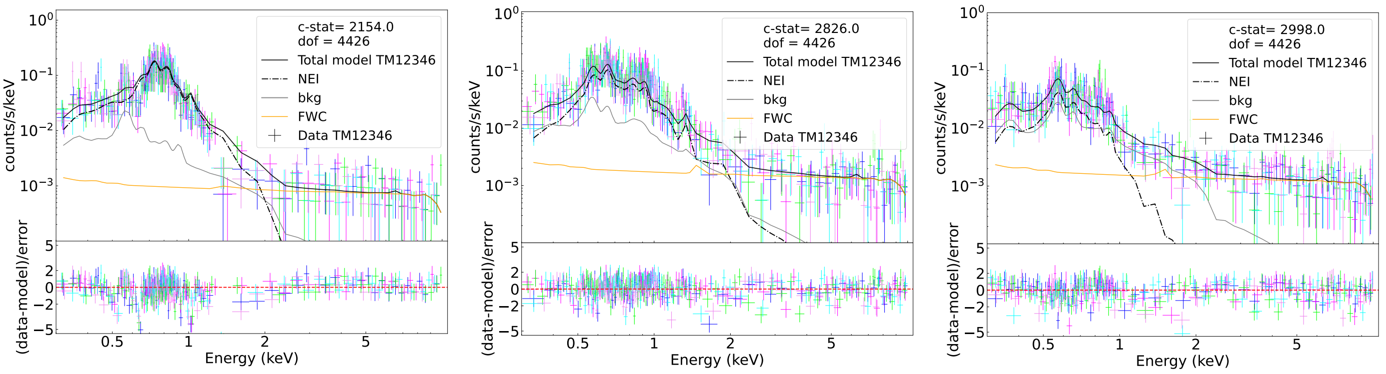

(d) J0454-6713 **(e) J0455-6839** **(f) J0456-6533**

Fig. C.1. eROSITA spectra with best-fit spectra. The coloured cross show the spectra of TM 1,2,3,4 and 6. The solid black lines show the total model (source + background), while the dot-dashed lines show the contribution of the SNR as one or multiple NEI components. The grey solid lines show the compound background model, while the orange solid lines show the contribution of the instrumental and particle background.

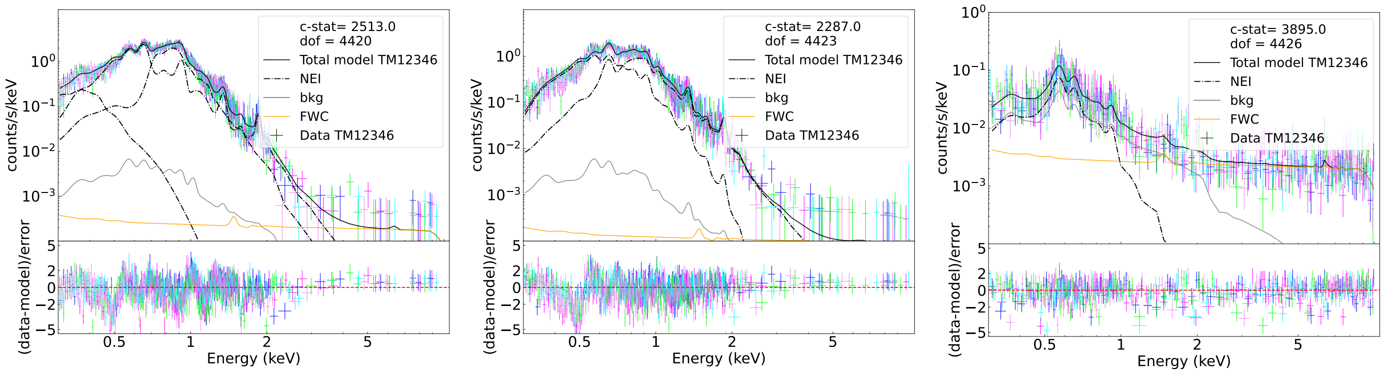

(a) J0505-6753

(b) J0505-6802

(c) J0506-6541

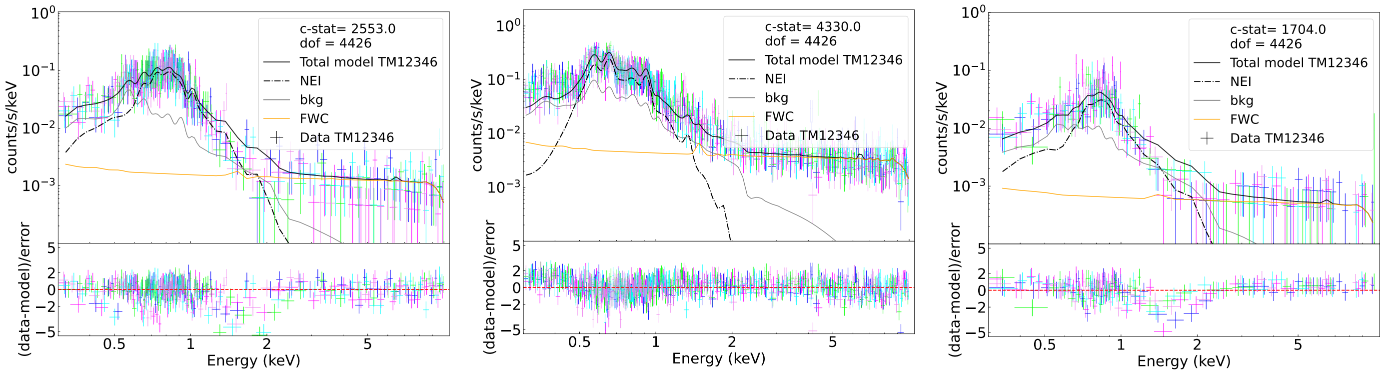

(d) J0506-7026

(e) J0507-6847

(f) J0508-6902

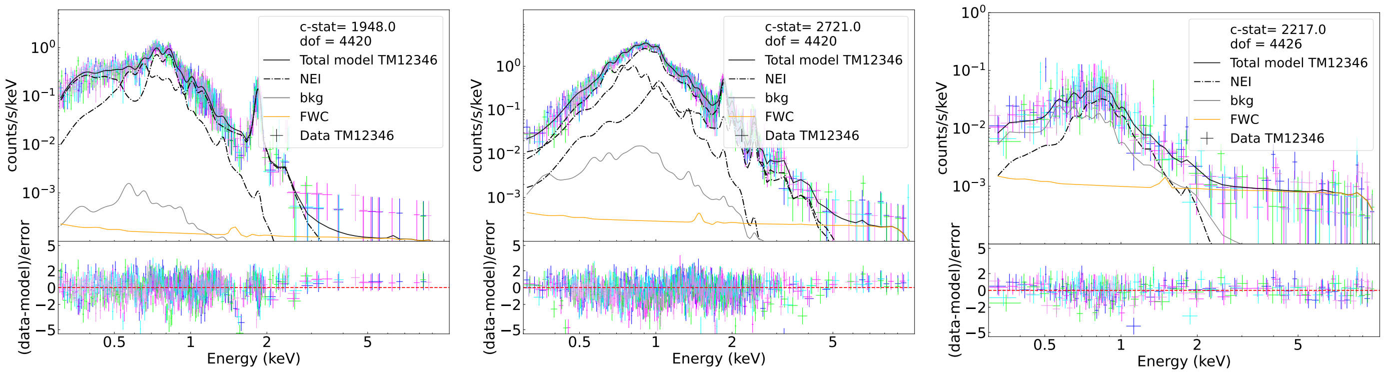

(g) J0509-6731

(h) J0509-6844

(i) J0513-6912

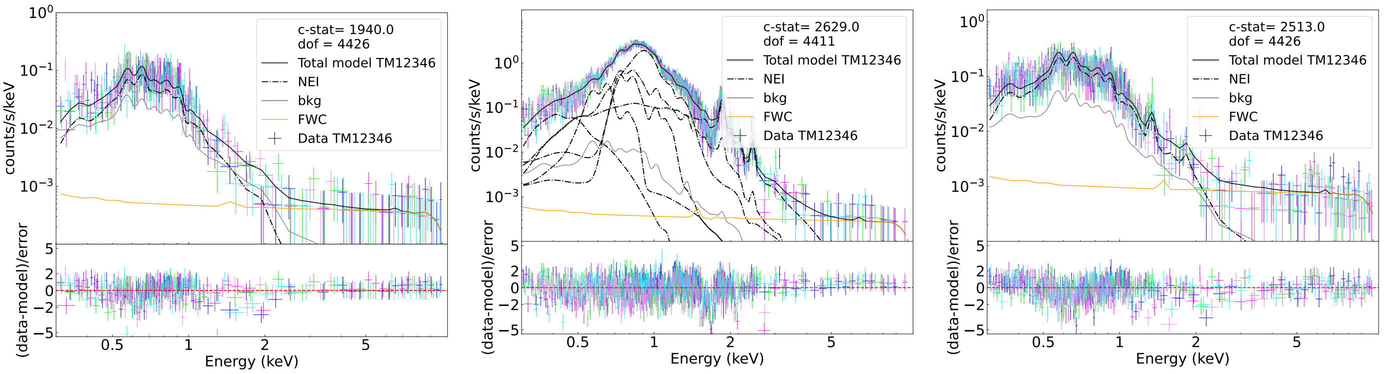

(j) J0518-6939

(k) J0519-6902

(l) J0519-6926

Fig. C.2. eROSITA spectra with best-fit spectra. The coloured cross show the spectra of TM 1,2,3,4 and 6. The solid black lines show the total model (source + background), while the dot-dashed lines show the contribution of the SNR as one or multiple NEI components. The grey solid lines show the compound background model, while the orange solid lines show the contribution of the instrumental and particle background.

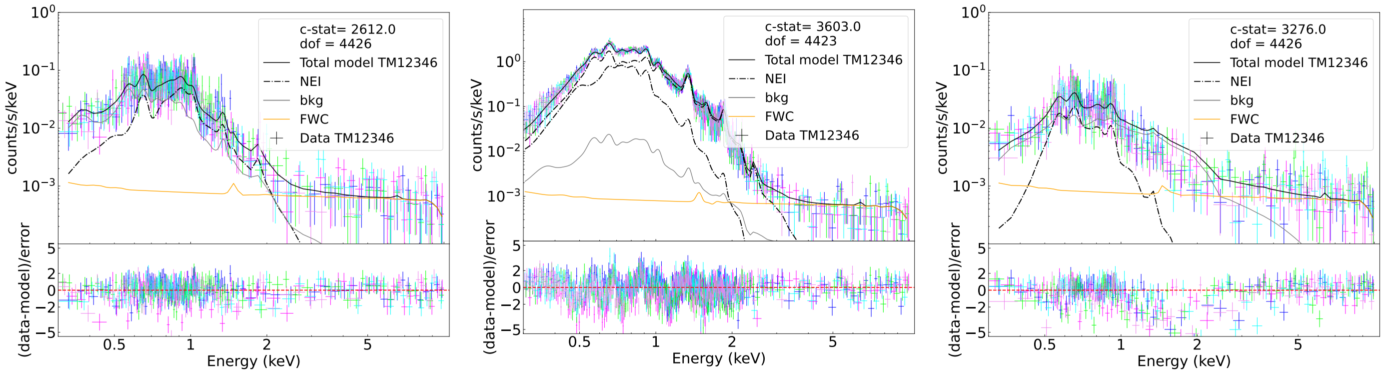

(a) J0523-6753

(b) J0525-6559

(c) J0525-6621

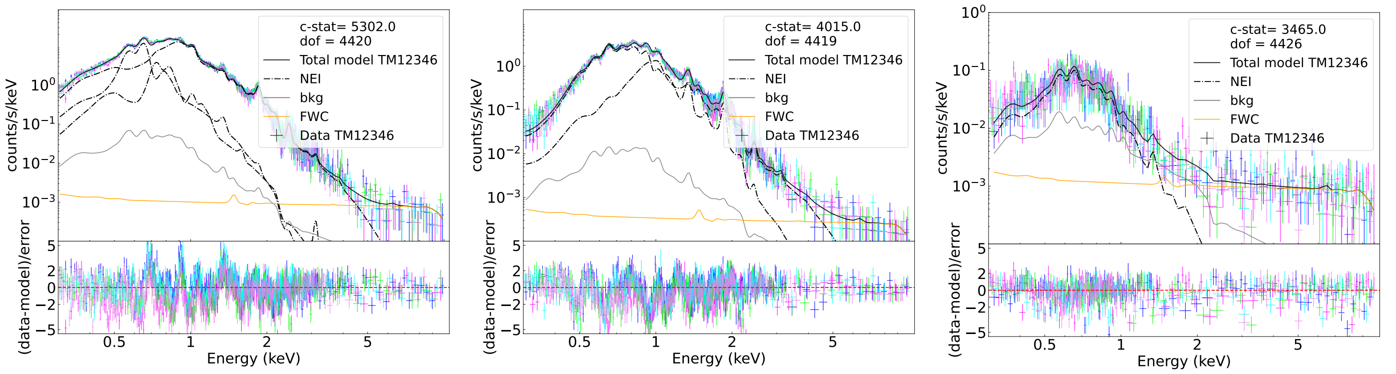

(d) J0525-6938

(e) J0526-6605

(f) J0527-6550

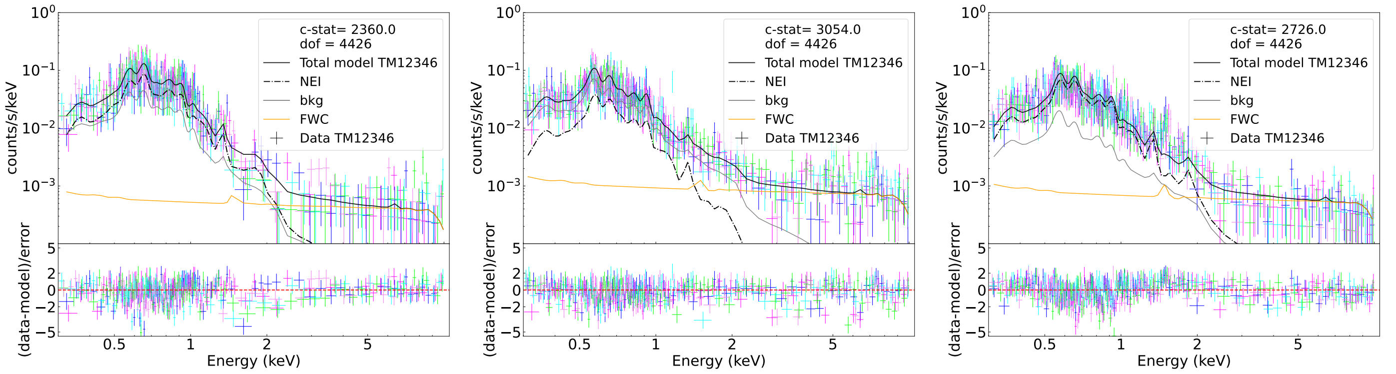

(g) J0527-6912

(h) J0528-6727

(i) J0529-6653

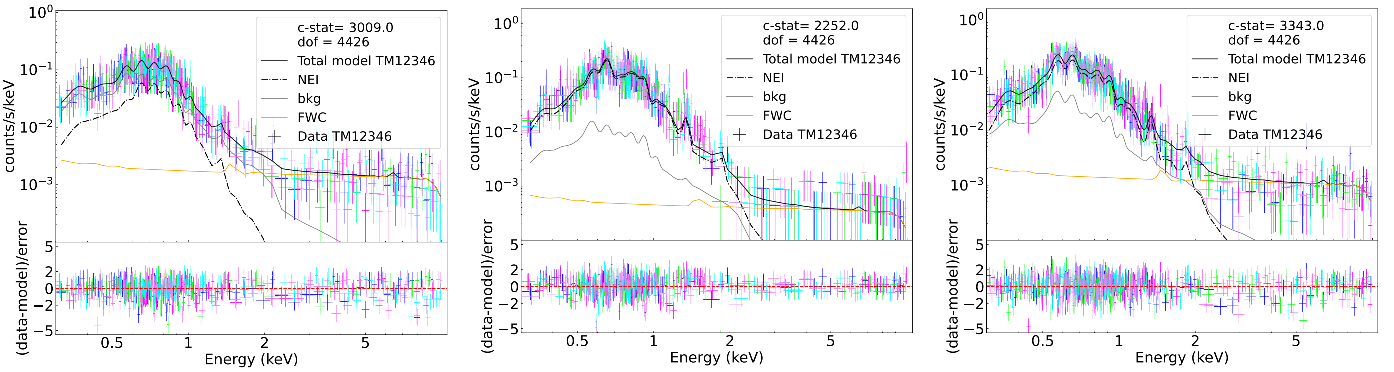

(j) J0530-7008

(k) J0531-7100

(l) J0532-6732

Fig. C.3. eROSITA spectra with best-fit spectra. The coloured cross show the spectra of TM 1,2,3,4 and 6. The solid black lines show the total model (source + background), while the dot-dashed lines show the contribution of the SNR as one or multiple NEI components. The grey solid lines show the compound background model, while the orange solid lines show the contribution of the instrumental and particle background.

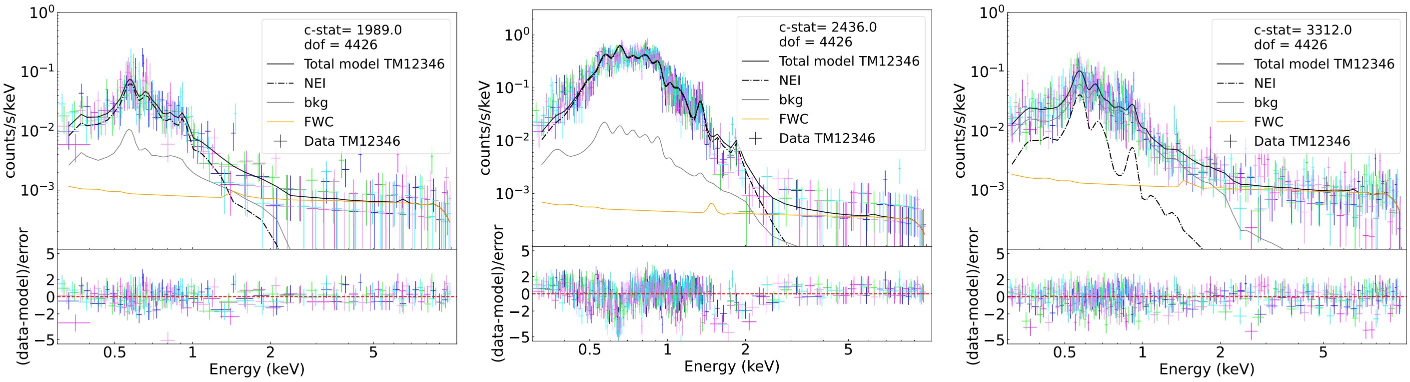

(a) J0533-7202 **(b) J0534-6955** **(c) J0534-6720**

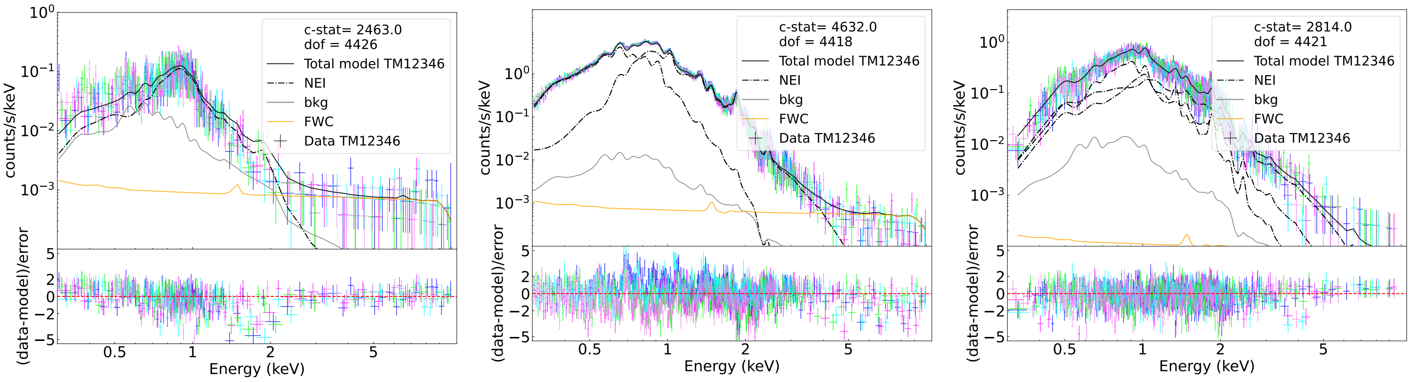

(d) J0534-7033 **(e) J0535-6602** **(f) J0535-6916**

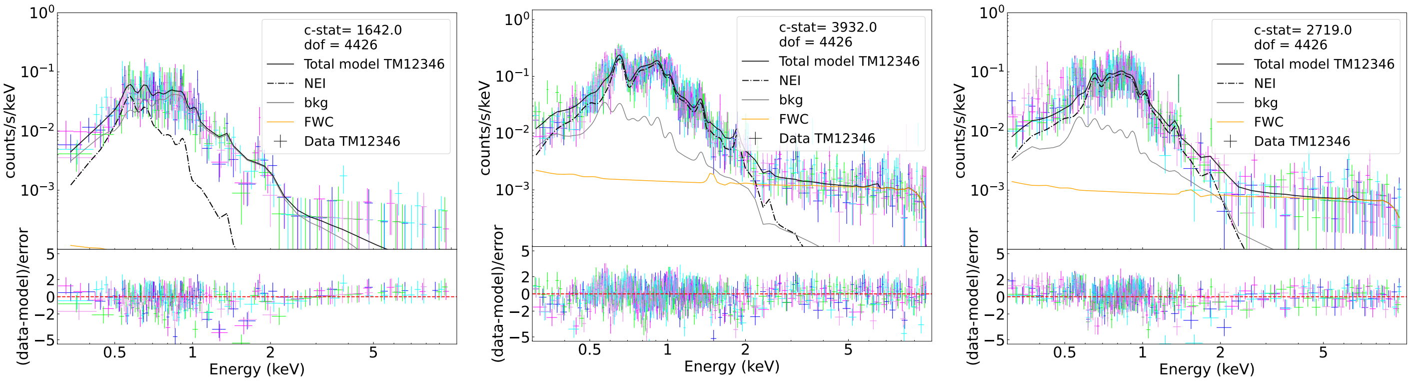

(g) J0535-6918 **(h) J0536-6735** **(i) J0536-7039**

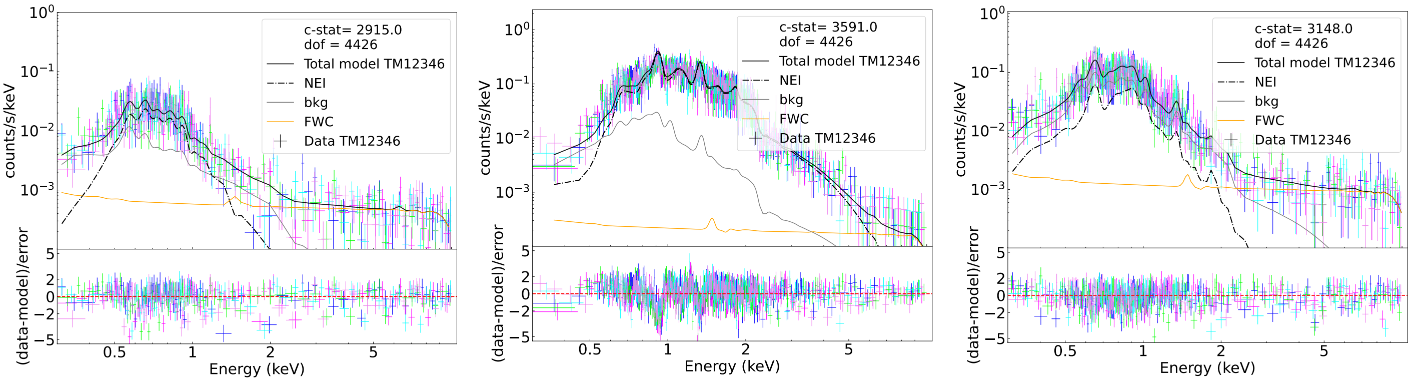

(j) J0537-6628 **(k) J0537-6910** **(l) J0538-6921**

Fig. C.4. eROSITA spectra with best-fit spectra. The coloured cross show the spectra of TM 1,2,3,4 and 6. The solid black lines show the total model (source + background), while the dot-dashed lines show the contribution of the SNR as one or multiple NEI components. The grey solid lines show the compound background model, while the orange solid lines show the contribution of the instrumental and particle background.

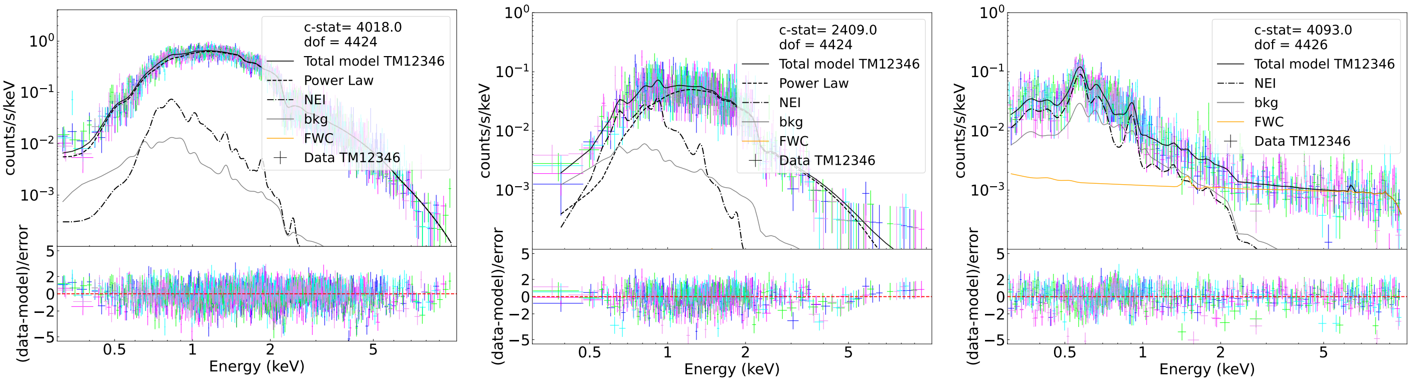

(a) J0540-6920 **(b) J0540-6944** **(c) J0541-6659**

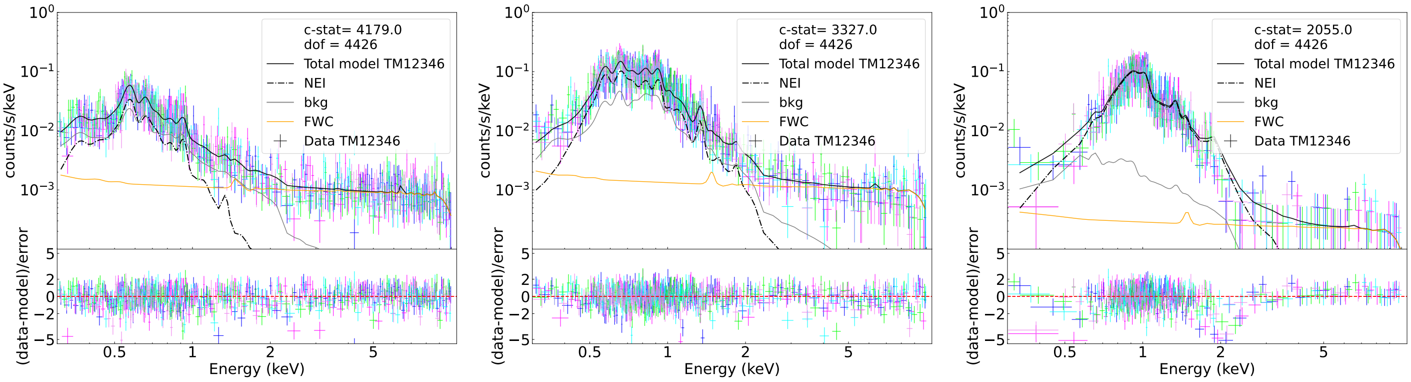

(d) J0543-6624 **(e) J0543-6858** **(f) J0547-6941**

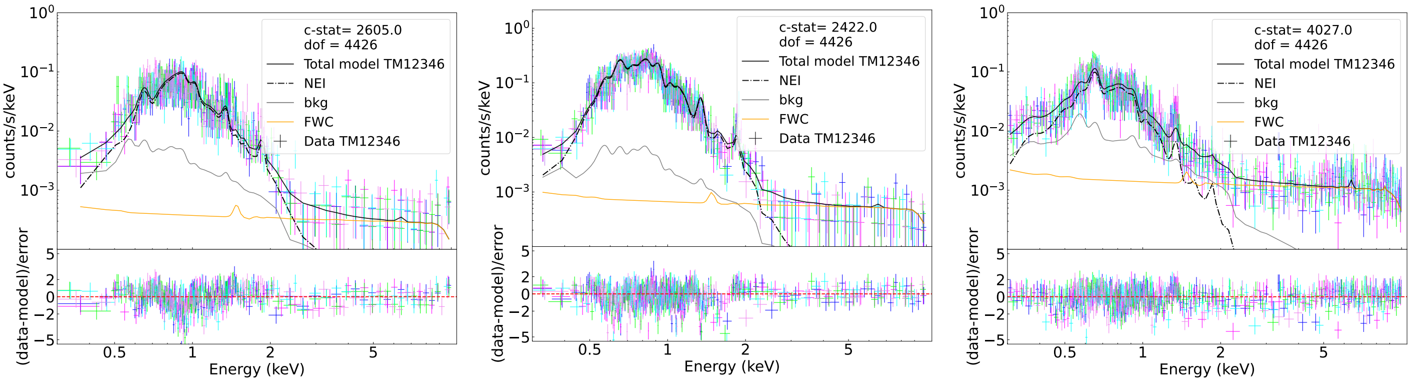

(g) J0547-6943 **(h) J0547-7025** **(i) J0550-6823**

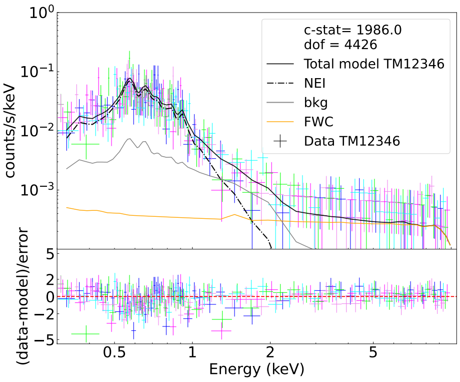

(j) J0614-7251

Fig. C.5. eROSITA spectra with best-fit spectra. The coloured cross show the spectra of TM 1,2,3,4 and 6. The solid black lines show the total model (source + background), while the dot-dashed lines show the contribution of the SNR as one or multiple NEI components. The grey solid lines show the compound background model, while the orange solid lines show the contribution of the instrumental and particle background.